aerospace

MDPI

Article

Constellation Optimization Design for Space-Based Optical Surveillance Based on Phase-Volume Coverage and Observation Geometry Quality Index

Xu Wu [1,2] and Pei Chen [1,2,*]

[1] School of Astronautics, Beihang University, Beijing 100191, China; wuxu@buaa.edu.cn
[2] Key Laboratory of Spacecraft Design Optimization and Dynamic Simulation Technology, Ministry of Education, Beijing 100191, China
* Correspondence: chenpei@buaa.edu.cn

Abstract

A fundamental challenge in space-based optical surveillance constellation design is the quantitative evaluation of coverage capability across the entire low-Earth-orbit (LEO) space. A phase-volume coverage model in the 4D (a, i, Ω, u) phase-space is proposed, and the multi-coverage ratio R_{multi}, mean covering satellite count $\bar{N}_{sat}$, and Observation Geometry Quality Index (OGQI) are introduced to overcome the limitations of single-metric coverage evaluation. A theoretical motivation for the relationship between OGQI components and orbit determination error covariance is provided via Fisher information matrix theory. Spherical-shell 3D spatial and phase-space 4D orbital frameworks are compared: the two frameworks are shown to be mathematically non-equivalent, and phase-space evaluation provides orbit-type-based diagnostic capability unavailable in spatial methods. Within the Walker-Delta framework with Sun-synchronous dawn–dusk orbits, camera pointing and constellation configuration are systematically optimized, yielding a preferred altitude of 1700 km and a $P = 6$-plane layout with coverage saturation at $T \geq 18$. Validation against the Space-Track TLE catalog (22,471 LEO objects) yields 95.49% coverage and 83.47% multi-coverage within a 1-h window. The phase-volume framework unifies coverage evaluation and constellation design in a common orbital element space, enabling systematic space-based optical surveillance constellation design.

Keywords: phase-volume coverage; observation geometry quality; Walker constellation; space-based optical surveillance; space situational awareness

Check for updates

Academic Editor: Paolo Tortora

Received: 1 July 2026
Revised: 27 July 2026
Accepted: 28 July 2026
Published: 31 July 2026

Copyright: © 2026 by the authors. Licensee MDPI, Basel, Switzerland. This article is an open access article distributed under the terms and conditions of the Creative Commons Attribution (CC BY) license.

1. Introduction

The population of low-Earth-orbit (LEO) space objects (here defined as orbital altitudes $h \in [200, 2400]$ km, covering the range from very low Earth orbit to the transition toward medium Earth orbit) has experienced explosive growth in recent years. Mega-constellations such as Starlink and OneWeb have deployed over ten thousand satellites [1], making LEO the region with the highest space-object density. According to a recent assessment by Mignocchi et al. [2], there are currently nearly 54,000 on-orbit space objects larger than 10 cm (including approximately 9300 active payloads), about 1.2 million debris fragments between 1 cm and 10 cm, and approximately 130 million micro-debris fragments between 1 mm and 1 cm. Faced with such an enormous target population, existing space surveillance capabilities rely predominantly on ground-based radar and ground-based optical systems. Ground-based optical systems are severely constrained by atmospheric absorption, weather

conditions, ionospheric disturbances, and geographic location. These constraints make continuous all-time, all-weather monitoring difficult to achieve. Radar systems, although capable of all-weather operation, incur high construction and operational costs and have limited detection range [3]. In contrast, space-based optical surveillance offers the advantages of flexible deployment, broad coverage, and freedom from atmospheric and geographic constraints, making it a key enabler for autonomous monitoring of large-scale LEO target populations. However, a single space-based surveillance satellite has limited coverage area and tracking arc length. Continuous monitoring of large target populations is, therefore, infeasible with a single satellite. Multi-satellite cooperative surveillance constellations are, therefore, essential [4].

Constructing space-based surveillance constellations first requires solving the quantitative evaluation problem of coverage performance. Constellation coverage assessment methods have, therefore, been a long-standing research focus in astronautics. Conventional methods sample targets in 3D position space and compute the fraction of observable targets. This paradigm was established in early constellation design studies. Walker [5] derived optimal circular-orbit configurations from spherical coverage symmetry. Ballard [6] proposed Rosette constellations that extend the configuration design space. Rider [7] first formalized the Above-the-Horizon (ATH) problem, laying the geometric foundation for space-object surveillance. Hanson and Linden [8] further optimized constellation coverage performance in low-altitude regions.

The above classical studies established the geometric foundations of constellation coverage analysis. Building on this foundation, coverage optimization methods have advanced significantly across multiple domains. In Earth observation, relevant methods have evolved from analytical to numerical and from uniform to adaptive approaches. Dai et al. [9] analyzed continuous coverage characteristics of satellite constellations over ground regions. Han et al. [10] proposed hybrid optimization strategies that combine metaheuristics with geometric analysis. Zong and Kohani [11] optimized LEO constellations targeting global coverage within a single revisit period. He et al. [12] proposed reconfigurable constellation design for dynamic disaster monitoring response. Yang et al. [13] optimized mega-constellation configurations for uniform coverage and observation efficiency. Wang et al. [14] further explored federated multi-agent collaborative algorithms for on-orbit constellation intelligence, highlighting the growing role of distributed computation in constellation operations.

Unlike Earth observation, which emphasizes ground coverage, space-object surveillance shifts the evaluation target from the Earth's surface to non-cooperative objects in orbital space. In space-object surveillance, the core coverage evaluation problem becomes how to quantify constellation visibility over space target populations. Ali et al. [15] established an analytical model for LEO satellite visibility prediction. Ji and Zeng [16] proposed a method for spatial effective coverage analysis in space-based optical observation. Han et al. [17] developed a novel method for calculating satellite visibility for an arbitrary sensor field. Shakun et al. [18] performed a comparative analysis of global optical observability of satellites in LEO. Roh and De Weck [19] proposed a global visibility assessment method for uncatalogued resident space objects. Hu et al. [20] optimized multi-sensor pointing for visible-light observation of GEO, GTO, and MEO targets using an equatorial LEO satellite as platform. At the surveillance constellation system design level, Flohrer et al. [21] evaluated the feasibility of space-based optical architectures for space surveillance missions. Du et al. [22] designed SBSS constellations for LEO debris catalog maintenance. Du et al. [23] further investigated cataloging constellations for high-altitude small debris. Hu et al. [24] proposed a space-based pseudo-fixed-latitude observation mode based on GEO belt characteristics. Biria and Marchand [25] derived analytical SSA

constellation coverage performance assessments from the ATH problem. Sun et al. [26] improved ATH coverage computation efficiency under dual-altitude-band constraints via ring-based discretization. D'Anniballe et al. [27] performed preliminary design of LEO-coverage surveillance constellations under illumination constraints. Fu et al. [28] optimized Walker constellation configurations using RBF surrogate models for space target awareness, although sensor pointing adopted a fixed radial (R-direction) default orientation without pointing optimization. Li et al. [29] designed circular revisit orbits for single-target rapid-response missions.

The above studies evaluate coverage in 3D position space $\mathbb{R}^3$. Whether by spherical-shell sampling, ATH analysis, or ground-track optimization, the fundamental evaluation unit is the spatial position (x, y, z). Wu et al. [30] recently proposed the Ω-u phase-plane coverage method, which for the first time elevated the evaluation domain from 3D spatial coordinates to 2D orbital element space. Fixing the target semi-major axis a_M and inclination i_M, coverage is evaluated on a discrete (Ω, u) phase-plane grid. This advance inaugurated the paradigm of "evaluating coverage in orbital element space." The present work extends this phase-plane approach to the full 4D (a, i, Ω, u) phase-volume, enabling unified coverage evaluation over the entire LEO target population. Whereas the phase-plane method restricts evaluation to a single (a_M, i_M) target orbit, the phase-volume framework accommodates the range of LEO altitudes and inclinations. Coverage patterns differ markedly across targets at different orbits. The designer can, therefore, obtain a global view of the constellation's overall coverage capability over the LEO space.

Beyond limitations in the evaluation domain, the above studies are similarly deficient at the metric level. Biria and Marchand [25] noted that defining evaluation criteria for space-based SSA constellations is extremely difficult, yet is an unavoidable core problem in constellation design. Nevertheless, existing research focuses almost exclusively on coverage ratio, i.e., the single scalar metric of the fraction of targets covered. However, for space-based optical surveillance, the ultimate goal is precise orbit determination (OD) of targets. OD accuracy depends on observation geometry (multi-satellite intersection angles), multi-coverage capability (triangulation conditions), and observation arc distribution [31], not merely on whether a target is seen. Coverage ratio cannot distinguish between "one satellite seeing the target once" and "multiple satellites simultaneously observing the target from different angles." These two scenarios have fundamentally different implications for OD accuracy. Gong et al. [32] incorporated OD error as an optimization metric in formation multi-target passive tracking mission planning. However, at the constellation design level, studies introducing an OD quality dimension remain scarce.

To address the above deficiencies, the following contributions are made:

1. **Phase-volume coverage model:** The evaluation space is extended from the 2D (Ω, u) phase-plane to the 4D (a, i, Ω, u) phase-space. This enables unified constellation coverage evaluation over the full LEO target space with $h \in [200, 2400]$ km and $i \in [12.5^\circ, 103^\circ]$. Phase-volume adopts orbital elements as the evaluation domain and naturally embeds orbital mechanics constraints into coverage evaluation.
2. **Observation geometry quality index system:** The multi-coverage ratio R_{multi} (fraction of grid points covered by $\geq$2 satellites) and the mean number of covering satellites $\bar{N}_{sat}$ are introduced. These are synthesized into the composite Observation Geometry Quality Index (OGQI). Together they expand constellation optimization from a single coverage-ratio dimension to a 2D coverage–observation-geometry-quality evaluation framework.
3. **Camera configuration optimization:** Differential evolution (DE) is employed to optimize the number and pointing directions of cameras per satellite. Phase-volume

coverage serves as the optimization objective, and the result identifies the optimal balance between coverage performance and engineering feasibility.

The proposed methods are systematically validated using SSO dawn–dusk Walker-Delta constellations as the baseline. DE optimizes camera count and pointing. Parametric sweeps select the optimal satellite altitude and constellation configuration. Finally, time-domain coverage validation is conducted on the Space-Track public TLE catalog (3 March 2026, 22,471 LEO objects) over a 1-h window. A coverage of 95.49% is achieved.

The remainder of this paper is organized as follows. Section 2 establishes the phase-volume coverage model and observation geometry quality index system, including the definition of OGQI and its theoretical motivation based on the Fisher information matrix. Section 3 describes the simulation setup, covering constellation parameters, target space, visibility constraints, and computational workflow. Section 4 presents results and discussion, including camera optimization, altitude sweeps, constellation configuration sweeps, OD quality analysis, and TLE validation. Section 5 summarizes the main conclusions and outlines future work.

Table 1 provides a glossary of the key symbols used throughout this paper.

Table 1. List of key symbols used throughout the paper.

Symbol	Definition	Unit
Orbital elements (surveillance satellite)		
a_G, i_G, Ω_G, u_G	Semi-major axis, inclination, RAAN, argument of latitude	km, deg, deg, deg
h	Satellite altitude ($h = a_G - R_\oplus$)	km
Orbital elements (target)		
a_M, i_M, Ω_M, u_M	Semi-major axis, inclination, RAAN, argument of latitude	km, deg, deg, deg
Constellation parameters		
P, S, T, F	Number of planes, satellites per plane, total satellites, phasing factor	–
Coverage metrics		
P_{vol}	Phase-volume coverage ratio	–
R_{multi}	Multi-coverage ratio (fraction of covered points with $\geq$2 satellites)	–
$\bar{N}_{sat}$	Mean number of covering satellites per covered grid point	–
OGQI	Observation Geometry Quality Index	–
σ_{rel}	Relative standard deviation of P_{vol} across (a, i) bins	–
Physical constants		
$R_\oplus$	Earth mean radius (6371 km)	km
μ	Earth gravitational constant (3.986×10^{14})	m^3/s^2
J_2	Second zonal harmonic coefficient (1.0826×10^{-3})	–
Camera and sensor		
θ_{FOV}	Camera field-of-view half-angle	deg
n_{cam}	Number of cameras per satellite	–
Vectors and positions		
$\mathbf{r}_s, \mathbf{r}_t$	Satellite and target position vectors (ECI)	m
$\mathbf{R}_\odot, \mathbf{r}_{moon}$	Sun and Moon position vectors (ECI)	m

2. Methodology

2.1. Phase-Volume Coverage Model

The mathematical model of phase-volume coverage is established in this section. The formulation starts from the phase-plane coverage of Wu et al. [30] and extends it to the 4D (a, i, Ω, u) phase-space, yielding a coverage measure over the full orbital element domain. The essential differences between phase-volume methods and spatial spherical-shell sampling are then systematically analyzed from three perspectives: orbital mechanics constraints, physical interpretability of metrics, and statistical distribution assumptions.

Terminological note. Throughout this paper, **phase-space** denotes the abstract 4D orbital element space (a, i, Ω, u) in which targets reside. **Phase-plane** refers to the 2D (Ω, u) plane at fixed semi-major axis a and inclination i (as introduced by Wu et al. [30]). **Phase-volume** refers to the coverage measure and evaluation methodology defined over the full (a, i, Ω, u) phase-space.

2.1.1. From Phase-Plane to Phase-Volume

For a target orbit (a_M, i_M), the phase-plane coverage [30], where a_M is the target semi-major axis and i_M is the target inclination, is given by:

$$P_{cov}(a_M, i_M) = \frac{1}{4\pi^2} \iint_0^{2\pi} \mathbb{I}_{cov}(\Omega_M, u_M \mid a_M, i_M)\, d\Omega_M\, du_M \tag{1}$$

where Ω_M is the target right ascension of ascending node (RAAN), u_M is the target argument of latitude, and $\mathbb{I}_{cov}(\cdot)$ is the coverage indicator function, taking the value 1 when at least one satellite can observe a target located at (Ω_M, u_M).

Phase-volume coverage extends this metric over the target semi-major axis a_M and inclination i_M space:

$$P_{vol} = \frac{1}{V_{LEO}} \iiiint \mathbb{I}_{cov}(a, i, \Omega, u)\, da\, di\, d\Omega\, du \tag{2}$$

where V_{LEO} is the phase-volume of the considered LEO space, with integration domain: $a \in [R_e + 200\ \text{km}, R_e + 2400\ \text{km}]$, $i \in [12.5^\circ, 103^\circ]$, $\Omega, u \in [0, 2\pi]$.

In practical computation, the target space is discretized into a grid of $n_a \times n_i \times n_\Omega \times n_u$ cells:

$$P_{vol} \approx \frac{1}{n_a n_i n_\Omega n_u} \sum_a \sum_i \sum_\Omega \sum_u \mathbb{I}_{cov}(a, i, \Omega, u) \tag{3}$$

2.1.2. Fundamental Differences Between Phase-Volume and Spatial Spherical-Shell Sampling

An intuitive alternative is to distribute target points uniformly in 3D space (e.g., on an Earth-centered sphere or within spatial voxels) [16], and directly evaluate the constellation's coverage over that point set. This spatial sampling approach differs fundamentally from the phase-volume method:

(1) Natural embedding of orbital mechanics constraints.

The fundamental problem with spatial spherical-shell sampling is that it operates in 3D position space $\mathbb{R}^3$, whereas the physics of space-based surveillance unfolds in 6D orbital element space $\mathbb{R}^6$. The mapping from orbital elements to spatial position is surjective rather than injective, and this information loss is the mathematical root of all limitations of spatial sampling methods.

For circular orbits (eccentricity $e = 0$), the instantaneous spatial position of a target is uniquely determined by its orbital elements:

$$\mathbf{r}(a, i, \Omega, u) = a \cdot \underbrace{\begin{bmatrix} \cos\Omega & -\sin\Omega & 0 \\ \sin\Omega & \cos\Omega & 0 \\ 0 & 0 & 1 \end{bmatrix}}_{R_z(\Omega)} \underbrace{\begin{bmatrix} 1 & 0 & 0 \\ 0 & \cos i & -\sin i \\ 0 & \sin i & \cos i \end{bmatrix}}_{R_x(i)} \begin{bmatrix} \cos u \\ \sin u \\ 0 \end{bmatrix} \tag{4}$$

i.e., $\mathbf{r} : (a, i, \Omega, u) \mapsto (x, y, z)$, a mapping from a 4D manifold to 3D space.

The inverse problem, i.e., determining a target's orbital elements given its spatial position $\mathbf{r}_0$, is underdetermined:

$$\{(a, i, \Omega, u) : \mathbf{r}(a, i, \Omega, u) = \mathbf{r}_0\} \tag{5}$$

is a 1D manifold in 3D space (infinitely many solutions). The same spatial position can correspond to different orbital inclinations and planes, each with distinct observation geometry, yet spatial sampling assigns them identical weight.

The phase-volume method directly adopts (a, i, Ω, u) as the evaluation domain. Its core advantage is that the dimensionality of the evaluation domain matches the physical degrees of freedom:

- a (semi-major axis): orbital period $T = 2\pi\sqrt{a^3/\mu}$ ($\mu = 3.986 \times 10^{14}$ m^3/s^2, Earth's gravitational constant), which determines the target's drift rate in the Ω-u plane.
- i (inclination): angle between the orbital plane and the equatorial plane, which determines the latitudinal extent of the target's ground track.
- Ω (RAAN): orientation of the orbital plane in inertial space, subject to secular J_2 precession ($J_2 = 1.0826 \times 10^{-3}$, Earth's second zonal harmonic coefficient).
- u (argument of latitude): instantaneous phase of the target along its orbit. At time t, $u(t) = u_0 + n(t - t_0)$, where n is the mean motion and u_0 the initial argument of latitude.

These four dimensions possess clear physical meaning, and their individual dynamical evolution laws are well characterized, endowing coverage evaluation with rigorous interpretability within the framework of orbital mechanics.

(2) Physical interpretability of evaluation metrics.

The spatial spherical-shell coverage ratio answers "what fraction of Earth's LEO volume can the constellation cover," while the phase-volume coverage ratio answers "what fraction of LEO target orbital states can the constellation cover." For space-based surveillance missions, the latter is closer to the true requirement. Targets are distributed along orbits rather than in space, and a surveillance satellite's coverage capability depends on the relative geometry between target and surveillance orbits. For example, the Ω difference determines overflight timing, while the i difference determines the orbital plane intersection angle. These relationships are more naturally expressed in orbital element space.

(3) Distinction between spatial and phase-space uniformity, and natural mapping to constellation design.

An implicit assumption of spatial spherical-shell sampling is that targets are isotropically distributed in space. However, the actual orbital distribution of LEO targets is strongly non-uniform. This can be rigorously illustrated through the Jacobian of the coordinate transformation from orbital elements to position space. Under the circular orbit assumption, the relationship between the target probability density in space $p_{xyz}(\mathbf{r})$ and that in orbital element space $p_{oe}(a, i, \Omega, u)$ is:

$$p_{xyz}(\mathbf{r})\, d^3\mathbf{r} = p_{oe}(a, i, \Omega) \underbrace{\left|\frac{\partial(x, y, z)}{\partial(a, i, \Omega)}\right|_{u\,\text{fixed}}}_{\mathcal{J}} da\, di\, d\Omega \tag{6}$$

Since Equation (4) maps from four orbital elements to three spatial coordinates, the transformation is not square. A well-defined 3×3 Jacobian determinant is obtained by fixing u and considering the mapping $(a, i, \Omega) \mapsto (x, y, z)$ at constant u. The full determinant evaluates to $|\det \mathbf{J}| = a^2 |\cos i| \cdot |\sin u|$ (see Appendix A). Under the assumption

that u is uniformly distributed over $[0, 2\pi)$, the u-dependent factor $|\sin u|$ averages to $\frac{1}{2\pi}\int_0^{2\pi}|\sin u|\,du = 2/\pi$, yielding the effective weighting factor:

$$\bar{\mathcal{J}} \equiv \mathbb{E}_u[|\det \mathbf{J}|] \propto a^2|\cos i| \tag{7}$$

Equation (7) is a conditional result: it holds under the specific assumption of uniform u-distribution and circular orbits. Different distributions of u (e.g., non-uniform sampling in time or orbital phase) would yield different averaging factors. This assumption is consistent with the phase-volume formulation, where u is uniformly gridded in $[0, 2\pi)$. The key qualitative conclusion, that spatial uniformity corresponds to non-uniform weighting in orbital element space, is independent of the specific normalization. Spatially uniform sampling is, therefore, non-uniform in orbital element space: polar orbits ($\cos i \to 0$) are severely under-sampled, while equatorial orbits ($\cos i \to 1$) are over-sampled. The a^2 factor further over-samples high-altitude targets relative to low-altitude targets. In orbital element space, a spatially uniform distribution corresponds to a weighting factor $w \propto \mathcal{J} \propto a^2|\cos i|$ per grid cell. Phase-space uniform evaluation uses $w \propto 1$ (each orbital type equally weighted). The two conventions differ by 1–2 pp (Section 4.1), reflecting different definitions of uniformity. Sphere-uniform evaluation and phase-space-uniform evaluation are not two implementations of the same quantity; only evaluation in orbital element space provides orbit-type-based diagnostic information.

A further advantage of the phase-space framework is its natural alignment with constellation design. Walker-Delta constellations are parameterized by (P, S, F) and satellite orbits by $(a_G, i_G, \Omega_G, u_G)$—all defined in orbital element space. Evaluating coverage in the same space makes the mapping between design parameters and performance direct. For example, changing the Walker F factor primarily affects the u-phase distribution of satellites, which can be directly observed in the (Ω, u) coverage pattern without geometric back-transformation.

In summary, the phase-volume method improves upon spatial evaluation in three dimensions: the evaluation domain aligns with orbital physics, the statistical interpretation distinguishes spatial from orbital-type uniformity, and the design feedback operates directly in the parameter space of constellation design.

2.2. Observation Geometry Quality Index

An observation geometry quality index system that transcends single-metric coverage evaluation is constructed in this section. First, the two foundational metrics, namely the multi-coverage ratio R_{multi} and the mean number of covering satellites $\bar{N}_{sat}$, are defined. These are then synthesized into the composite Observation Geometry Quality Index (OGQI). Subsequently, the Fisher information matrix of optical angle measurements is used to provide a theoretical motivation for the qualitative relationship between each OGQI component and OD geometry quality. The analysis illustrates how each aggregate metric correlates with OD convergence trends at the constellation level, without claiming to predict the OD accuracy for individual targets. A four-regime convergence–divergence partition is presented. Finally, the engineering rationale of the OGQI design is discussed.

2.2.1. Multi-Coverage Ratio R_{multi}

For each grid point in the phase-volume, define the covering satellite count $n_{cov}(a, i, \Omega, u) \in \{0, 1, \ldots, T\}$. The multi-coverage ratio is the fraction of covered grid points simultaneously observed by at least two satellites:

$$R_{multi} = \frac{|\{(a, i, \Omega, u) : n_{cov} \geq 2\}|}{|\{(a, i, \Omega, u) : n_{cov} \geq 1\}|} \tag{8}$$

R_{multi} reflects the constellation's triangulation capability: multiple satellites simultaneously observing the same target from different angles is a prerequisite for single-pass orbit determination.

2.2.2. Mean Number of Covering Satellites $\bar{N}_{sat}$

$$\bar{N}_{sat} = \frac{1}{N_{covered}} \sum_{(a,i,\Omega,u)\in\mathcal{C}} n_{cov}(a,i,\Omega,u) \tag{9}$$

where $\mathcal{C}$ is the set of covered grid points. $\bar{N}_{sat}$ reflects the "redundancy" of coverage.

2.2.3. Observation Geometry Quality Index (OGQI)

Integrating the above metrics, the Observation Geometry Quality Index is defined as:

$$\text{OGQI} = P_{vol} \times (1 + \alpha R_{multi} + \beta \bar{N}_{sat,norm}) \times \frac{1}{1 + \gamma \cdot \sigma_{rel}} \tag{10}$$

where:

- P_{vol}: phase-volume coverage ratio (fundamental detection capability);
- R_{multi}: multi-coverage ratio (triangulation potential);
- $\bar{N}_{sat,norm} = \bar{N}_{sat}/T$: normalized mean number of covering satellites;
- $\sigma_{rel} = \sigma(P_{vol})/\bar{P}_{vol}$: relative standard deviation of phase-volume coverage across (a,i) bins (uniformity penalty: a large σ_{rel} indicates that some orbital regions are significantly under-covered relative to others. The value of σ_{rel} is reported wherever OGQI is tabulated);
- $\alpha = 0.5$, $\beta = 0.3$, $\gamma = 0.3$: weighting coefficients.

OGQI is designed as an engineering criterion (engineering criterion) that synthesizes multiple coverage-geometry dimensions into a single figure of merit for constellation optimization. The design philosophy of OGQI is that an excellent constellation should simultaneously possess high coverage (capable of detecting targets), high multi-coverage ratio (capable of triangulation), and high uniformity (consistent performance across all target orbit types).

The OGQI definition is a weighted combination of coverage geometry metrics, with weighting coefficients (α, β, γ) that reflect the designer's preference among coverage, multi-coverage, and uniformity. The choice of these coefficients is application-dependent; a sensitivity analysis of OGQI rankings to $\pm 30\%$ variations in α and β is provided in Section 4.5, confirming that the optimal configuration selection is robust within this range. In the following, the Fisher information matrix of optical angle measurements is used to provide theoretical motivation for each OGQI component and its relationship to the OD error covariance matrix $\mathbf{P}$, offering physical insight into why these geometric metrics matter for orbit determination.

2.2.4. Optical Angle Measurement Model and Fisher Information Matrix

For a single observation epoch t_k, with target state $\mathbf{x} = [\mathbf{r}^T, \mathbf{v}^T]^T \in \mathbb{R}^6$ (where $\mathbf{r}$ is the position vector and $\mathbf{v}$ the velocity vector), and N_{sat} surveillance satellites simultaneously providing optical angle measurements (N_{sat} is the number of satellites visible to the target, distinct from the constellation-averaged $\bar{N}_{sat}$). The measurement from the j-th satellite consists of azimuth Az_j and elevation El_j:

$$\mathbf{z}_j = \begin{bmatrix} Az_j \\ El_j \end{bmatrix} = \begin{bmatrix} \arctan 2(\mathbf{u}_j \cdot \mathbf{e}_y^{cam},\ \mathbf{u}_j \cdot \mathbf{e}_x^{cam}) \\ \arcsin(\mathbf{u}_j \cdot \mathbf{e}_z^{cam}) \end{bmatrix} + \boldsymbol{\varepsilon}_j, \quad \boldsymbol{\varepsilon}_j \sim \mathcal{N}(0, \sigma_{meas}^2 \mathbf{I}_2) \tag{11}$$

where $\mathbf{u}_j = (\mathbf{r} - \mathbf{r}_{s,j})/\|\mathbf{r} - \mathbf{r}_{s,j}\|$ is the line-of-sight (LOS) unit vector, $\mathbf{r}_{s,j}$ is the position vector of the j-th surveillance satellite, $\{\mathbf{e}_x^{cam}, \mathbf{e}_y^{cam}, \mathbf{e}_z^{cam}\}$ are the camera coordinate system basis vectors, $\mathbf{I}_2$ is the 2×2 identity matrix (each angle measurement is independent and identically distributed), $\sigma_{meas} = 2\theta_{FOV}/4000 \approx 8.73 \times 10^{-5}$ rad is the single-pixel angular resolution, and $\theta_{FOV} = 10^\circ$ is the camera field-of-view half-angle.

Measurement Jacobian

For a single epoch, the Jacobian of the angle measurements with respect to the target position $\mathbf{r}$ is:

$$\mathbf{H}_{pos}^{(j)} = \frac{\partial(Az_j, El_j)}{\partial \mathbf{r}} = \frac{\partial(Az_j, El_j)}{\partial \mathbf{u}_j} \cdot \frac{1}{\rho_j}(\mathbf{I}_3 - \mathbf{u}_j \mathbf{u}_j^T) \in \mathbb{R}^{2\times 3} \tag{12}$$

where $\rho_j = \|\mathbf{r} - \mathbf{r}_{s,j}\|$ is the satellite-to-target range. $\partial \mathbf{u}_j/\partial \mathbf{r} = (1/\rho_j)(\mathbf{I}_3 - \mathbf{u}_j \mathbf{u}_j^T)$ is the derivative of the unit LOS vector with respect to the target position ($\mathbf{I}_3$ is the 3×3 identity matrix), projecting any vector onto the plane perpendicular to the LOS.

The key insight is that at a single epoch, angle measurements have no direct sensitivity to velocity, i.e., $\partial(Az_j, El_j)/\partial \mathbf{v} = \mathbf{0}_{2\times 3}$ ($\mathbf{0}_{2\times 3}$ denotes the 2×3 zero matrix). Hence the full 6D Jacobian for a single epoch is $\mathbf{H}^{(j)} = [\mathbf{H}_{pos}^{(j)},\ \mathbf{0}_{2\times 3}]$, whose row rank does not exceed 2.

Position Fisher Information Matrix

For simultaneous observations by N_{sat} satellites, the Fisher information matrix of the position components is:

$$\mathbf{J}_{pos} = \frac{1}{\sigma_{meas}^2} \sum_{j=1}^{N_{sat}} {\mathbf{H}_{pos}^{(j)}}^T \mathbf{H}_{pos}^{(j)} \in \mathbb{R}^{3\times 3} \tag{13}$$

Rank Analysis and Triangulation Condition

Each camera provides two angle measurements, $\text{rank}(\mathbf{H}_{pos}^{(j)}) \leq 2$. The full-rank condition for $\mathbf{J}_{pos}$ from N_{sat} satellites is:

$$\text{rank}(\mathbf{J}_{pos}) = \begin{cases} \leq 2, & N_{sat} = 1 \quad \text{(3D position indeterminate. Position error covariance } \mathbf{P}_{pos} \text{ diverges)} \\ = 3 \text{ (attainable)}, & N_{sat} \geq 2 \quad \text{(triangulation feasible)} \end{cases} \tag{14}$$

Therefore, $N_{sat} \geq 2$ is the necessary condition for instantaneous position triangulation. This directly endows the multi-coverage ratio R_{multi} with a clear physical meaning: R_{multi} quantifies the proportion of targets in phase-space that satisfy the triangulation condition.

Complete 6D Orbit Determination

Velocity components must be obtained through multi-epoch position differencing: if the target position is determined at two or more epochs via triangulation, the state transition equation $\mathbf{r}_{k+1} = \mathbf{\Phi}_{rr}\mathbf{r}_k + \mathbf{\Phi}_{rv}\mathbf{v}_k$ (where $\mathbf{\Phi}_{rr}$ and $\mathbf{\Phi}_{rv}$ are the position–position and position–velocity sub-blocks of the two-body state transition matrix $\mathbf{\Phi}(t_{k+1}, t_k)$) renders $\mathbf{v}$ observable. Thus, $N_{sat} \geq 2$ is a key enabling condition for short-arc orbit determination.

2.2.5. Qualitative Covariance Scaling Relation

When $\mathbf{J}_{pos}$ is full-rank, the position error covariance is $\mathbf{P}_{pos} = \mathbf{J}_{pos}^{-1}$. The following scaling relation is a conceptual engineering model that captures the qualitative trends of how aggregate coverage metrics correlate with OD error levels. It is not a predictive formula for individual targets: the actual covariance for any specific target depends on the

line-of-sight geometry of the observing satellites, not solely on the count-based metrics R_{multi} and $\bar{N}_{sat}$.

$$\mathrm{tr}(\mathbf{P}_{pos}) \sim \frac{\sigma_{meas}^2 \bar{\rho}^2}{\bar{N}_{sat}} \cdot \Gamma(R_{multi}) \tag{15}$$

where $\bar{\rho}$ is the typical satellite-to-target range, $\sim$ denotes qualitative proportionality (trend-level correspondence, not exact equality), and the geometric degradation factor $\Gamma(R_{multi})$ is a conceptual indicator of multi-satellite observation geometry quality:

$$\Gamma(R_{multi}) = \begin{cases} \text{diverges}, & R_{multi} \to 0 \quad \text{(single-satellite observations only; } \mathbf{J}_{pos} \text{ rank-deficient)} \\ \text{well-conditioned}, & R_{multi} \geq 0.5 \quad \text{(sufficient multi-satellite coverage)} \end{cases} \tag{16}$$

The engineering interpretation of Equation (15) is qualitative rather than quantitative:

1. Role of $\bar{N}_{sat}$ (trend-level): Greater satellite redundancy is associated with lower position error, consistent with the $1/\bar{N}_{sat}$ scaling of information averaging. However, $\bar{N}_{sat}$ is an aggregate metric averaged over all covered targets. The actual information gain for a given target depends on the specific lines of sight of the covering satellites.
2. Role of R_{multi} (enabling condition): The multi-coverage ratio indicates the fraction of targets with at least two simultaneous observations, a necessary statistical precondition for triangulation at the constellation level. It is not a sufficient condition for any individual target, since parallel or near-parallel lines of sight can leave $\mathbf{J}_{pos}$ ill-conditioned even when $N_{sat} \geq 2$.
3. Role of P_{vol} (opportunity): The coverage ratio determines the existence of observation opportunities. When $P_{vol} \to 0$, $\mathbf{J}_{pos} \equiv \mathbf{0}$ for the vast majority of targets.

2.2.6. Four-Regime Partition of OD Convergence–Divergence

The qualitative scaling of Equation (15) motivates a four-regime engineering partition of OD convergence behavior in the (P_{vol}, R_{multi}) plane, as summarized in Table 2. These regimes are qualitative engineering interpretations of constellation-level OD capability, not predictive criteria for individual target OD accuracy:

Table 2. Qualitative four-regime partition of OD convergence and divergence. The thresholds are order-of-magnitude engineering estimates based on aggregate coverage metrics (P_{vol}, R_{multi}, $\bar{N}_{sat}$). They serve as a qualitative engineering interpretation of constellation-level OD capability, not as predictive criteria for individual target OD accuracy. $\mathrm{tr}(\mathbf{P}_{pos})$ is in km^2; $\sqrt{\mathrm{tr}(\mathbf{P}_{pos})}$ gives position error std. dev. in km.

Regime	Condition	Physical Meaning	$\mathrm{tr}(\mathbf{P}_{pos})$ Order
Divergent	$P_{vol} < 0.1$ or $R_{multi} < 0.2$	Very sparse coverage or single-satellite observations only. $\mathbf{J}_{pos}$ nearly rank-deficient. OD infeasible	>100 km^2
Transition	$0.1 \leq P_{vol} < 0.5$ and $R_{multi} \geq 0.2$	Partial coverage with some triangulation capability. Longer arcs (5–10 min) required for convergence	1–100 km^2
Convergent	$P_{vol} \geq 0.5$, $R_{multi} \geq 0.5$, $\bar{N}_{sat} \geq 2$	Sufficient multi-satellite coverage. $\mathbf{J}_{pos}$ full-rank and well-conditioned. Supports short-arc OD (10–60 s)	<1 km^2
High-Precision	$P_{vol} \geq 0.8$, $R_{multi} \geq 0.7$, $\bar{N}_{sat} \geq 3$	Near-instantaneous OD conditions. Highly redundant multi-angle observations	<0.01 km^2

2.2.7. Theoretical Motivation for the OGQI Design

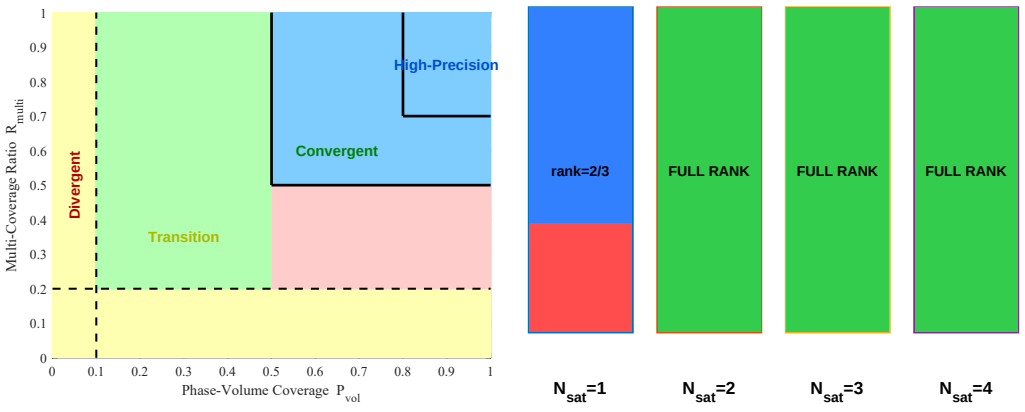
The Fisher information matrix analysis provides theoretical motivation for each OGQI component, though the relationship is qualitative rather than a strict mathematical equivalence:

1. P_{vol} (coverage ratio) determines whether observation information is obtained for a given target. Higher coverage means a larger fraction of targets with non-zero information.
2. R_{multi} (multi-coverage ratio) reflects the fraction of covered targets observed by at least two satellites. For a given target, simultaneous observations from satellites with non-collinear lines of sight (LOS) can make the position FIM full rank. However, $N_{sat} \geq 2$ alone does not guarantee full rank: parallel or anti-parallel LOS geometries remain rank-deficient, and near-parallel geometries may be full rank but severely ill-conditioned. Therefore, R_{multi} provides a statistical indication of triangulation potential at the constellation level, rather than a guarantee of OD feasibility for every individual target.
3. $\bar{N}_{sat}$ (mean number of covering satellites) represents observation redundancy. Under favorable geometry, the position covariance scales approximately as $1/\bar{N}_{sat}$, motivating the inclusion of $\bar{N}_{sat}$ as a quality-enhancing factor.
4. σ_{rel} (relative standard deviation) reflects the spatial uniformity of coverage. A large σ_{rel} implies that some orbital regions are significantly under-covered relative to others, leading to locally degraded OD conditions.

In summary, the OGQI components are positively correlated with favorable OD geometry at the constellation level, but this relationship is qualitative. R_{multi} and $\bar{N}_{sat}$ are aggregate count-based metrics. They indicate statistical potential for good OD geometry but cannot predict the actual FIM or covariance for any individual target, which depends on the specific lines of sight. The OGQI should be interpreted as a qualitative engineering index for comparing constellation designs, not as a predictive OD accuracy metric. Validation through multi-epoch angles-only OD Monte Carlo simulation is left for future work.

The coefficient $\alpha = 0.5$ for R_{multi} exceeds $\beta = 0.3$ for $\bar{N}_{sat,norm}$, reflecting the designer's judgment that triangulation potential (rank condition) carries greater weight than observation redundancy (magnitude enhancement). Optimization should prioritize configurations with high R_{multi} before pursuing marginal gains in P_{vol} and $\bar{N}_{sat}$. A sensitivity analysis of the OGQI ranking to variations in (α, β) is provided in Section 4.5.

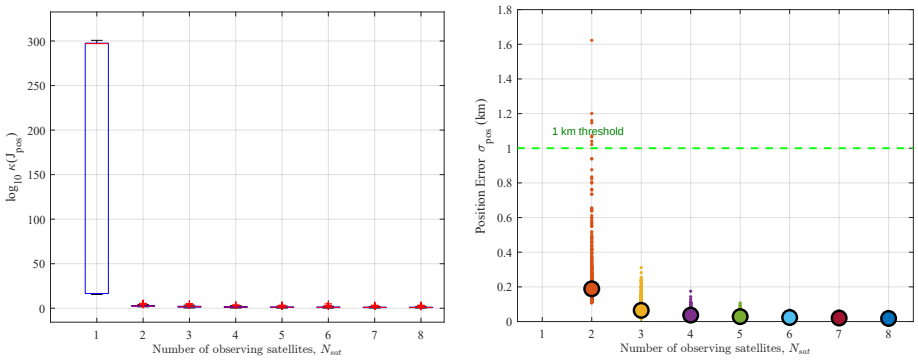
Figure 1 illustrates the four-regime partition of OD convergence in the (P_{vol}, R_{multi}) plane. Figure 1a maps the four OD convergence regimes in the (P_{vol}, R_{multi}) plane. Figure 1b illustrates the rank transition of $\mathbf{J}_{pos}$ across the $N_{sat} = 2$ triangulation threshold. The regime map is a qualitative engineering tool for comparing constellation designs. It does not predict OD accuracy for individual targets.



(**a**) (**b**)

Figure 1. Qualitative orbit determination regime partition and Fisher information matrix analysis. (**a**) (P_{vol}, R_{multi}) regime map showing the four OD convergence regimes as a qualitative engineering interpretation. (**b**) Rank of $\mathbf{J}_{pos}(3 \times 3)$ as a function of N_{sat}.

Figure 2 numerically validates, via purely geometric Monte Carlo simulations (500 random observation geometries per group), the condition number and expected 3D position error of $\mathbf{J}_{pos}$ as functions of N_{sat}, confirming the sharp transition to a well-conditioned regime at $N_{sat} \geq 2$. In the figures, condition numbers are stratified into three categories: well-conditioned ($\kappa < 100$), moderately ill-conditioned ($100 \leq \kappa < 1000$), and severely ill-conditioned ($\kappa \geq 1000$), rather than applying a binary full-rank/deficient label. Cases with $N_{sat} = 2$ but nearly parallel lines of sight may be full-rank yet severely ill-conditioned, as discussed in Section 2.



(**a**) (**b**)

Figure 2. Purely geometric Monte Carlo validation: variation of the position Fisher information matrix with the number of simultaneous observing satellites. (**a**) $\log_{10}$ condition number. (**b**) Expected 3D position error σ_{pos}.

Figure 3 applies the optimal constellation ($P = 6, S = 4, T = 24$, 5 cameras, $h = 1700$ km SSO) determined in Section 4. The (a, i, Ω, u) phase-space is sampled to compute the condition number of $\mathbf{J}_{pos}$ for each target. The results verify that the conclusions from the purely geometric Monte Carlo analysis hold under the actual constellation geometry. The condition number distribution stratified by target altitude reveals pronounced spatial non-uniformity of coverage quality. Low-altitude targets ($h < 500$ km) have systematically higher condition numbers due to fewer visible satellites and poorer observation geometry, while mid-altitude targets ($h \approx 800$–1400 km) enjoy the best observation geometry. This indicates that OD quality depends not only on constellation configuration but also on target orbital altitude, providing a theoretical basis for the subsequent altitude sweeps and configuration optimization.

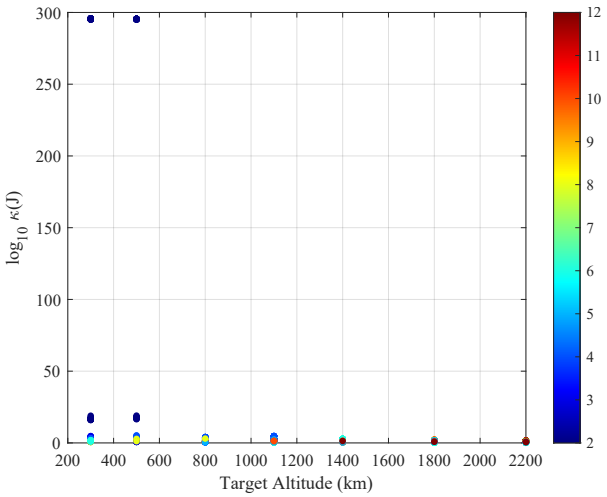


Figure 3. Actual constellation simulation validation: condition number of the position Fisher information matrix stratified by target altitude, under the optimal constellation configuration ($T = 24$, $P = 6$, $S = 4$, $F = 0$, 5 cameras, $h = 1700$ km SSO).

3. Simulation Setup

3.1. Constellation Parameters

- Orbit type: SSO dawn–dusk orbit. The inclination is determined by the J_2 perturbation condition.
- Satellite altitude: $h = 600$–2500 km. Primary results use $h = 1700$ km (phase-volume optimal altitude) as the baseline.
- Constellation configuration: Walker-Delta (P, S, F), with $P \in \{1, 2, 3, 4, 6\}$, $S \in \{1, 2, 3, 4, 6\}$, $F \in [0, P-1]$.
- Cameras: 3–8 cameras. Five cameras serve as the engineering baseline, representing a typical payload configuration for this class of satellite that balances mass, power, and coverage capability. The pure-coverage optimum is 8 cameras, with the Stage 2 camera-count validation confirming 5 as the comprehensive optimum. FOV half-angle 10°, detector array 4000 × 4000 pixels, angular rate constraint 3–120 pix/s.

3.2. Target Space

- Altitude range: 300, 500, 800, 1100, 1400, 1800, 2200 km (7 layers).
- Inclination range: 20°, 35°, 53°, 70°, 85°, 97° (6 bins).
- Ω-u grid: Coarse grid 18×18, fine grid 36×36.
- Total phase-volume grid points: $7 \times 6 \times 18 \times 18 = 13,608$ (coarse grid).

3.3. Visibility Constraints

For each target–satellite pair, all of the following constraints must be satisfied for the target to be declared visible:

(1) Earth shadow constraint.

The target must be in sunlight, not occulted by the Earth (cylindrical Earth shadow model). Let $\mathbf{R}_\odot$ be the Sun position, $\mathbf{r}_t$ the target position, $R_\oplus = 6371$ km the Earth radius. The target enters shadow when $\|\mathbf{r}_t\| \cos\theta < 0$ and $\|\mathbf{r}_t\| \sin\theta < R_\oplus$, where θ is the target–Earth–Sun angle.

(2) Earth occultation constraint.

From the surveillance satellite's perspective, the target must lie above the Earth's limb. Accounting for atmospheric occultation of optical observations, the effective limb altitude is taken as $R_\oplus + h_{atm}$, where $h_{atm} = 100$ km is the effective atmospheric thickness [33]:

$$d_{min} = \frac{\|\mathbf{r}_s \times (\mathbf{r}_t - \mathbf{r}_s)\|}{\|\mathbf{r}_t - \mathbf{r}_s\|} = \|\mathbf{r}_s\| \cdot \sin(\theta_{limb}) > R_\oplus + h_{atm}, \quad \theta_{limb} = \arccos\left(\frac{-\mathbf{r}_s \cdot (\mathbf{r}_t - \mathbf{r}_s)}{\|\mathbf{r}_s\| \cdot \|\mathbf{r}_t - \mathbf{r}_s\|}\right) \tag{17}$$

where $\mathbf{r}_s$ is the satellite position, θ_{limb} is the angle between the satellite-to-Earth-center vector $(-\mathbf{r}_s)$ and the satellite-to-target vector $(\mathbf{r}_t - \mathbf{r}_s)$, and d_{min} is the minimum perpendicular distance from the Earth's center to the line of sight.

(3) Earth albedo (glare) avoidance constraint.

To avoid interference from scattered light off the Earth's atmosphere (Earth albedo/glare) and the bright Earth background, the angle between the LOS and the Earth's limb must exceed the glare avoidance angle $\alpha_{glare} = 5°$ [34]:

$$\theta_{limb} - \arcsin(R_\oplus / \|\mathbf{r}_s\|) \geq \alpha_{glare} \tag{18}$$

(4) Sun avoidance constraint.

To prevent the target signal from being overwhelmed by direct sunlight during backlit observations, the angle between the LOS and the Sun direction must be less than 90° (i.e., when the target–satellite–Sun angle exceeds 90°, the target is in the shadowed hemisphere and cannot be observed). Additionally, to prevent the Sun from entering the camera FOV and causing detector saturation or damage, the angle between each camera optical axis and the Sun direction must be at least 30° [34]:

$$\angle(\mathbf{r}_s - \mathbf{r}_t,\ \mathbf{R}_\odot - \mathbf{r}_t) < 90^\circ, \quad \min_k \angle(\mathbf{e}_{cam}^{(k)},\ \mathbf{R}_\odot - \mathbf{r}_s) \geq 30^\circ \tag{19}$$

(5) Moon avoidance constraint.

To prevent bright lunar background interference with target detection, the target–Moon angle must be at least 10°; additionally, to prevent stray light interference from the Moon entering the camera FOV, the angle between each camera optical axis and the Moon direction must be at least 10° [34]:

$$\angle(\mathbf{r}_t - \mathbf{r}_s,\ \mathbf{r}_{moon} - \mathbf{r}_s) \geq 10^\circ, \quad \min_k \angle(\mathbf{e}_{cam}^{(k)},\ \mathbf{r}_{moon} - \mathbf{r}_s) \geq 10^\circ \tag{20}$$

where $\mathbf{r}_{moon}$ is the Moon position vector.

(6) Field-of-view constraint.

The target must fall within the square FOV of at least one camera. Each camera FOV is 20° × 20° (half-angle 10°):

$$|\Delta Az| \leq \theta_{FOV}, \quad |\Delta El| \leq \theta_{FOV}, \quad \theta_{FOV} = 10^\circ \tag{21}$$

where ΔAz and ΔEl are the deviations of the target LOS direction from the camera boresight in azimuth and elevation, respectively.

(7) Angular rate constraint.

The relative angular rate of the target on the focal plane must fall within the detector's trackable range:

$$\omega_{min} \leq \omega_{rel} \leq \omega_{max}, \quad \omega_{min} = 3\ \text{pix/s}, \ \ \omega_{max} = 120\ \text{pix/s} \tag{22}$$

The relative angular rate is $\omega_{rel} = \|\mathbf{v}_{rel,\perp}\| / \|\mathbf{r}_{rel}\|$, where $\mathbf{r}_{rel} = \mathbf{r}_t - \mathbf{r}_s$ is the satellite-to-target relative position vector, and $\mathbf{v}_{rel,\perp}$ is the component of the relative velocity perpendicular to the LOS. The pixel angular resolution is $2\theta_{FOV}/4000 = 8.73 \times 10^{-5}$ rad/pix.

(8) Dwell time constraint.

The target must remain continuously within a single camera's FOV for at least $T_{dwell} = 10$ s to satisfy the arc-length requirement for target detection and initial orbit determination. The phase-volume model evaluates instantaneous geometric visibility and does not directly incorporate a time-domain dwell constraint. The 10 s dwell time check is applied in the time-domain TLE validation (Section 4.6). Incorporating dwell time into the phase-volume framework is left for future work.

The solar, lunar, and Earth glare exclusion angles are adopted from values commonly used in the optical SSA literature [34]. The dwell time (10 s) and angular rate thresholds (3–120 pix/s) are based on engineering experience with typical CCD-based star trackers and space surveillance sensors. These visibility parameters are summarized in Table 3.

Table 3. Key symbols and values of the visibility model.

Symbol	Meaning	Value
$R_\oplus$	Earth mean radius	6371 km
θ_{FOV}	Camera FOV half-angle	10° (square 20° × 20°)
N_{pix}	Detector array	4000 × 4000 pixels
ω_{min}	Minimum trackable angular rate	3 pix/s
ω_{max}	Maximum trackable angular rate	120 pix/s
α_{glare}	Earth albedo avoidance angle	5°
α_{sun}	Camera Sun avoidance angle	30°
α_{moon}	Target and camera Moon avoidance angle	10°
T_{dwell}	Minimum dwell time	10 s
t_{sim}	Single simulation duration	3600 s (1 h)

3.4. Computing Environment

All simulations were performed on a workstation equipped with an Intel Core i7-10875H CPU (8 cores, 16 threads), 16 GB RAM, running Windows 10 (64-bit). Orbital propagation. Phase-volume grid evaluation uses a two-body Keplerian propagator with J_2 perturbation for RAAN and argument of perigee precession. TLE validation uses the SGP4 propagator with TLE-consistent dynamics. The Sun position is computed via an analytical ephemeris model [31].

Differential evolution (DE) settings. Camera pointing optimization uses a differential evolution (DE) algorithm with the parameters summarized in Table 4. The optimization objective is maximization of equal-weight phase-volume coverage P_{vol}. All eight candidate altitudes in the SSO altitude sweep use the same DE population and generation budget. Five independent DE runs are performed per configuration (see Table 4).

Computational complexity. The phase-volume coverage evaluation for a single satellite at a single camera pointing configuration involves $n_a \times n_i \times n_\Omega \times n_u = 13,608$ target grid points (coarse grid). Each grid-point evaluation requires visibility checks against 3–8 cameras. For a full constellation with T satellites, the complexity scales approximately as $O(n_a n_i n_\Omega n_u \, T \, n_{cam})$. A single altitude sweep (8 altitudes × 30 DE generations × 50 population) requires approximately 12,000 phase-volume evaluations. The constellation sweep over 74 (P, S, F) combinations requires approximately 74 evaluations per grid resolution.

Table 4. DE optimization and computational parameters.

Parameter	Value
DE variant	DE/rand/1/bin
Population size (NP)	30
Maximum generations	25
Mutation factor (F)	0.8
Crossover probability (CR)	0.85
Stopping criterion	No improvement in best fitness for 10 consecutive generations
Initialization	Warm start (uniform camera azimuths, nominal elevation)

3.5. Computational Workflow

The overall optimization workflow is illustrated in Figure 4 and consists of four stages: Detailed description of each stage:

1. SSO altitude sweep: Camera pointing is DE-optimized at each candidate altitude, using $n_{cam} = 5$ as the engineering baseline. The optimal altitude is selected by comparing single-satellite phase-volume coverage P_{vol}.

2. Camera count validation: At the optimal altitude, DE re-optimizes pointing for $n_{cam} = 3$–8, and the marginal coverage gain of each additional camera is evaluated on the fine grid.
3. Constellation configuration sweep: 74 Walker-Delta combinations (P, S, F) are evaluated at the selected altitude. The top-ranked configurations are identified by P_{vol} on the coarse grid.
4. OD quality assessment: For each top configuration, per-satellite coverage maps yield R_{multi}, $\bar{N}_{sat}$, and OGQI. Eight representative T values are further evaluated on the fine grid.

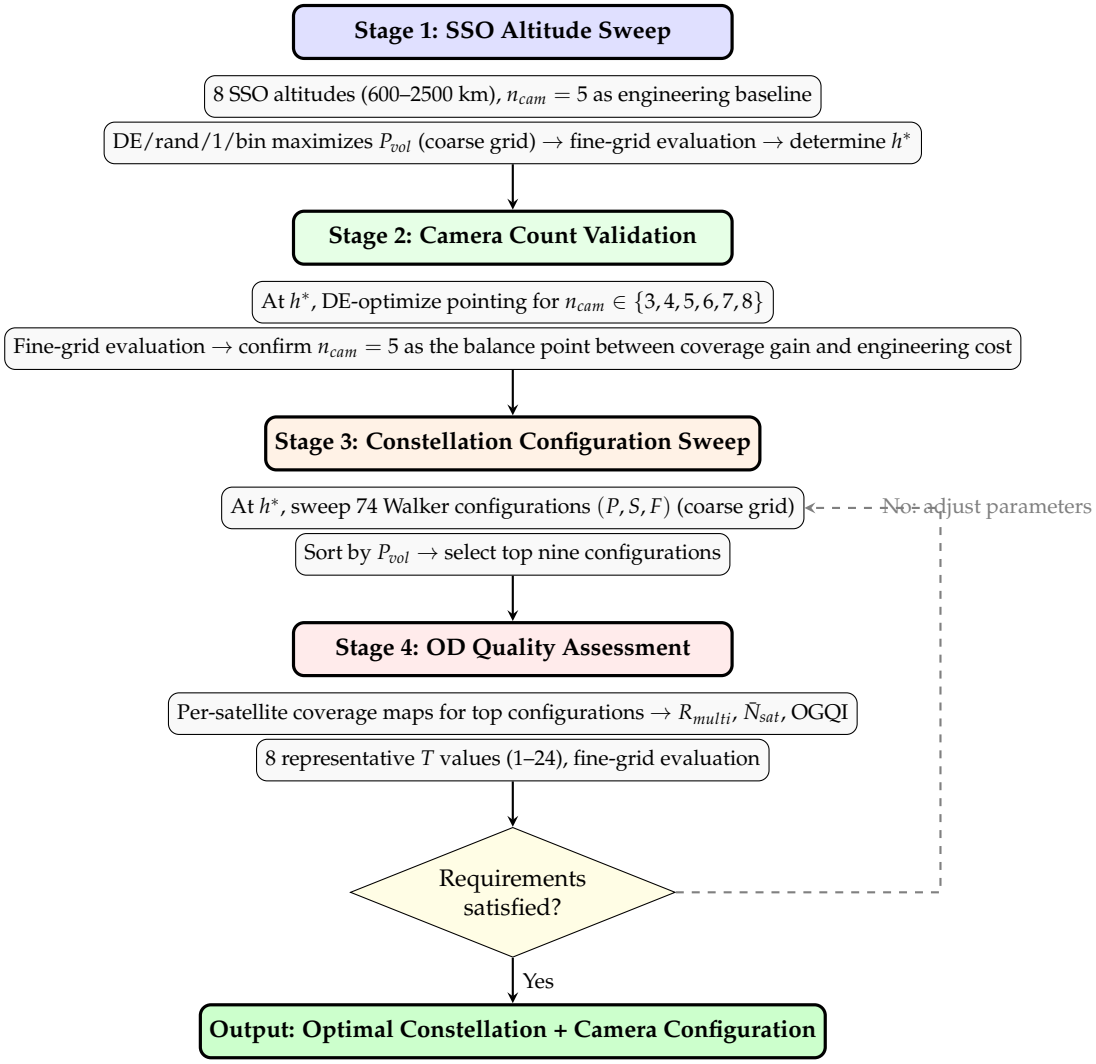


Figure 4. Flowchart of the joint constellation configuration and camera pointing optimization.

3.6. Camera Configuration Optimization

The number of cameras n_{cam} and their pointing angles $(Az_i, El_i)_{i=1}^{n_{cam}}$ are key design variables affecting coverage performance. The azimuth Az_i and elevation El_i are defined in the satellite Vehicle Velocity Local Horizontal (VVLH) coordinate frame: $Az = 0°$ points along the velocity direction, $Az = 90°$ points toward nadir, and El is measured from the local horizontal plane. The pointing angles of each camera are optimized via differential evolution (DE) for $n_{cam} \in \{3,4,5,6,7,8\}$, with phase-volume coverage maximization as the objective.

The optimization problem is formulated as:

$$\min_{\mathbf{x}\in\mathbb{R}^{2n_{cam}}} \left[1 - P_{vol}(\mathbf{x})\right], \quad \text{s.t. } Az_i \in [0, 2\pi],\ El_i \in [-\pi/2, \pi/2] \tag{23}$$

where $\mathbf{x} = [Az_1, El_1, \ldots, Az_{n_{cam}}, El_{n_{cam}}]^T$, and $P_{vol}(\mathbf{x})$ is the single-satellite phase-volume coverage ratio.

Differential evolution algorithm. The classical DE/rand/1/bin strategy [35] is adopted. The algorithm pseudocode is presented in Algorithm 1, with the following core operations:

Mutation: For each target vector $\mathbf{x}_i^{(g)}$ in the population, three mutually distinct individuals $\mathbf{x}_{r1}, \mathbf{x}_{r2}, \mathbf{x}_{r3}$ are randomly selected to generate a donor vector: $\mathbf{v}_i = \mathbf{x}_{r1} + F \cdot (\mathbf{x}_{r2} - \mathbf{x}_{r3})$, where the scaling factor $F = 0.7$.

Crossover: The donor vector and target vector undergo dimension-wise crossover to generate a trial vector $\mathbf{u}_i$: for each dimension j, $u_{i,j} = v_{i,j}$ if $\text{rand}(0,1) \leq CR$ or $j = j_{rand}$, otherwise $u_{i,j} = x_{i,j}$. Crossover probability $CR = 0.85$.

Selection: Greedy selection. If the trial vector $\mathbf{u}_i$ has better fitness than the target vector $\mathbf{x}_i$, then $\mathbf{x}_i^{(g+1)} = \mathbf{u}_i$. Otherwise $\mathbf{x}_i$ is retained.

Parameter settings: population size $NP = 30$, maximum generations $G_{max} = 25$–40 (depending on problem dimension), stall tolerance $tolStall = 5$–8 generations. DE is accelerated on a coarse target grid (3×3 (a, i) sample points), with final evaluation on the fine grid (7×6 (a, i) sample points). For each camera count n, the optimization is warm-started from the optimized solution of $n - 1$ cameras by inserting an additional camera with a randomly initialized pointing direction.

After optimization, the optimal pointing directions are applied to all constellation satellites for evaluation of constellation-level phase-volume coverage and OD quality.

Algorithm 1 DE/rand/1/bin

Input: NP, F, CR, G_{max}, bounds $[lb, ub]$
1. Randomly initialize population $\mathbf{X}^{(0)} \in [lb, ub]^{D \times NP}$
2. Evaluate fitness $f(\mathbf{x}_i)$ for all $i = 1, \ldots, NP$
3. **for** $g = 0$ **to** $G_{max} - 1$ **do**
   4. **for** $i = 1$ **to** NP **do**
      5. Randomly select $r_1 \neq r_2 \neq r_3 \neq i$
      6. $\mathbf{v}_i = \mathbf{x}_{r1} + F \cdot (\mathbf{x}_{r2} - \mathbf{x}_{r3})$ // mutation
      7. Randomly select $j_{rand} \in \{1, \ldots, D\}$
      8. **for** $j = 1$ **to** D **do** // crossover
         $u_{i,j} = v_{i,j}$ if rand $\leq CR$ or $j = j_{rand}$, else $u_{i,j} = x_{i,j}$
      9. $\mathbf{u}_i \leftarrow \text{clamp}(\mathbf{u}_i, lb, ub)$ // boundary correction
      10. **if** $f(\mathbf{u}_i) \leq f(\mathbf{x}_i)$ **then** $\mathbf{x}_i \leftarrow \mathbf{u}_i$ // selection
   11. **if** best solution stagnates $> tolStall$ generations **then break**

Output: $\mathbf{x}_{best} = \arg\min_i f(\mathbf{x}_i)$

4. Results and Discussion

Before proceeding to constellation optimization, Section 4.1 first compares spherical-shell (3D spatial) and phase-space (4D orbital) uniform sampling against TLE ground truth, establishing equal-weight phase-space as the evaluation baseline. The subsequent sections then follow the four-stage optimization workflow of Section 3 (Figure 4). Section 4.2 sweeps SSO altitude to identify the optimal orbital altitude. Section 4.3 validates the camera count selection at that altitude. Section 4.4 sweeps 74 Walker-Delta (P, S, F) configurations. Section 4.5 presents observation geometry quality index (OGQI) for the top configurations and analyzes coverage distribution in (a, i) space. Section 4.6 validates the final configuration against the Space-Track public TLE catalog in the time domain.

4.1. Empirical Comparative Validation of Phase-Volume and Spherical-Shell Frameworks

Before applying the phase-volume method to constellation design, it is necessary to verify whether the phase-space (4D orbital) framework genuinely outperforms the spherical-shell (3D spatial) counterpart, and to identify their fundamental differences in prediction accuracy and diagnostic capability. This section compares the two frameworks under an identical visibility model, using actual TLE targets as ground truth. The spherical-shell framework evaluates coverage by sampling target positions uniformly in $\mathbb{R}^3$, while the phase-space framework evaluates coverage by sampling target orbital elements uniformly in (a, i, Ω, u). As derived in Section 2 (Equation (6)), spatial uniformity corresponds to a weighting factor $w \propto a^2|\cos i|$ in orbital element space, making the two frameworks non-equivalent.

To quantitatively compare the two frameworks, a simple configuration independent of subsequent optimization is adopted (SSO satellite at $h = 1000$ km, 3 cameras with fixed pointing: along-track direction and $\pm 45°$ on each side, FOV half-angle 10°). Under an identical visibility model, the actual coverage of each of $N = 22,471$ TLE targets (filtered to $h \in [200, 2400]$ km, $i \in [12.5°, 103°]$, data downloaded from Space-Track (https://www.space-track.org on 3 March 2026)) is computed as ground truth, and the prediction accuracy of the two uniform weighting frameworks is compared. Figure 5 shows the distribution of LEO targets from this TLE catalog in (a, i) space.

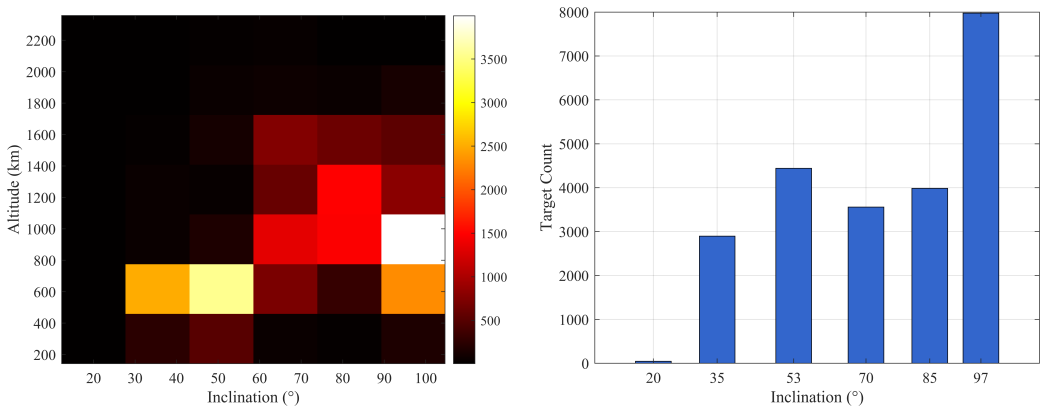


Figure 5. LEO target distribution in the TLE catalog: targets are heavily concentrated at $h = 500$–800 km (71.8% of the catalog), confirming the strong non-uniformity of the real LEO population. (**a**) (a, i)-space histogram. (**b**) Marginal distribution by inclination.

Figure 6 presents the weight distribution and prediction error comparison between the two frameworks. Figure 6a shows the spherical-shell uniform weight map in (a, i) space, Figure 6b the equal-weight phase-space counterpart, Figure 6c their difference highlighting the Jacobian bias, and Figure 6d the resulting TLE coverage prediction errors. The comparison reveals the following:

1. Both uniform frameworks systematically overestimate coverage relative to the TLE ground truth (0.86%). The spherical-shell prediction is +6.17 pp and the phase-space prediction is +4.61 pp. This systematic overestimation is expected. The TLE catalog is highly non-uniform, concentrated at specific orbital altitudes and inclinations. Neither uniform weighting scheme captures this empirical distribution. The 1.56 pp difference between the two predictions reflects their different weighting assumptions (spatial uniformity vs. orbital-type uniformity), not an accuracy advantage of one over the other. The Jacobian factor $\bar{\mathcal{J}} \propto a^2|\cos i|$ (under the uniform-u assumption, Equation (7)) governs the mapping between the two spaces: uniform sampling in 3D position space

over-weights equatorial targets and under-weights polar targets in orbital element space, while equal-weight phase-space treats all orbital types uniformly.

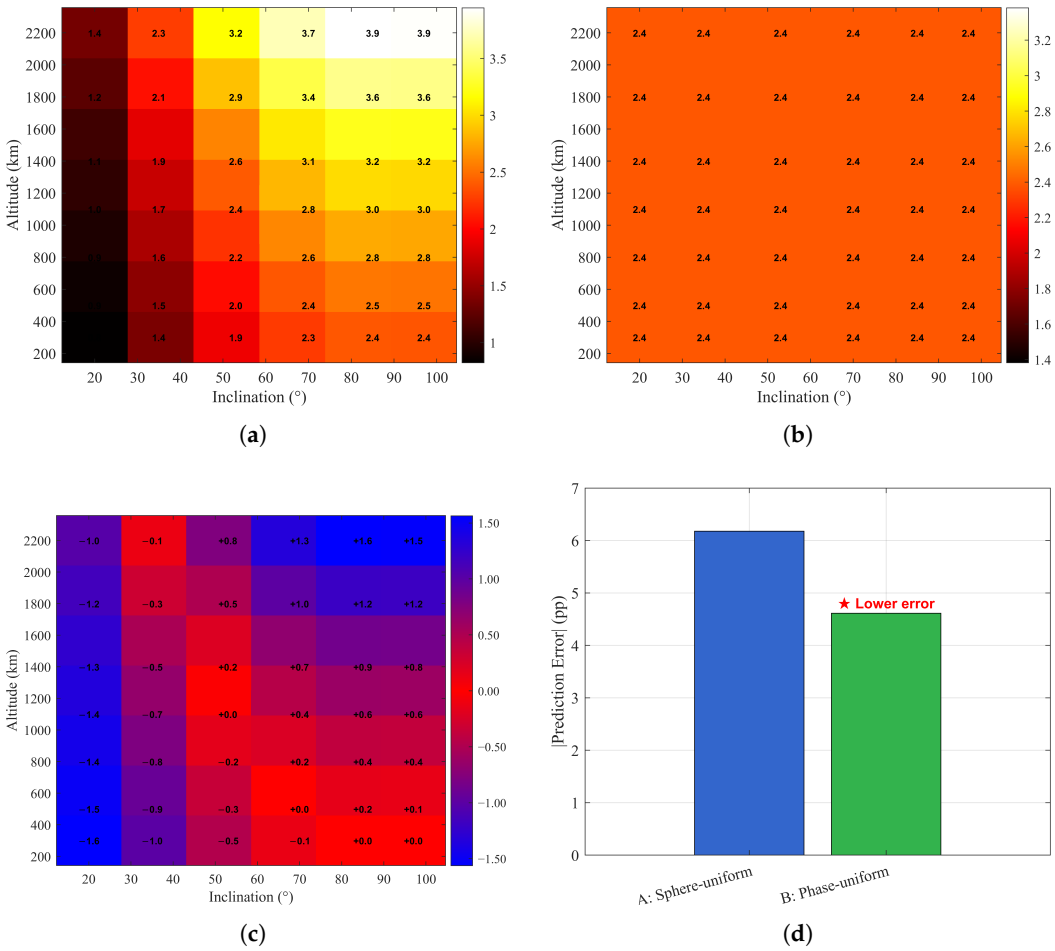


Figure 6. Weight distribution and prediction error comparison between spherical-shell and phase-space frameworks. (**a**) Sphere-uniform weights ($w \propto a^2|\cos i|$). (**b**) Phase-space uniform weights. (**c**) Weight difference (positive: sphere over-weights). (**d**) Prediction errors against TLE actual coverage.

2. The essential difference between the two frameworks is diagnostic in nature:
   - The spherical-shell framework produces coverage diagnostics as "coverage vs. latitude" curves. Each latitude band mixes multiple orbital types.
   - In contrast, the phase-space framework produces coverage diagnostics as a "coverage vs. (a, i)" matrix. Targets within each cell share consistent orbital geometry, and the diagnostic conclusion reads "coverage is lowest for targets at $h \approx 1400$ km and $i \approx 70°$". This is discussed further in the OGQI analysis of Section 4.5. The actionable recommendation is "optimize camera pointing for that specific orbital type". This diagnostic capability (the ability to identify which orbital types are poorly covered and why) is the defining advantage of phase-space evaluation, and is independent of whether the evaluation weights match the actual target distribution.
3. The comparison in Table 5 uses a simple configuration ($h = 1000$ km SSO, 3 fixed-pointing cameras) independent of subsequent DE optimization, demonstrating that the diagnostic advantage reflects an intrinsic property of the evaluation paradigm rather than any specific optimized design. Note that the phase-volume framework mathematically supports weighting by the actual target orbital distribution (empirical weighting), which would bring the predictions closer to the TLE ground truth. Empir-

ical weighting using TLE-derived (a, i) histograms is left for future work. The present study adopts equal-weight phase-space as a conservative design baseline for three reasons. First, the TLE catalog reflects the selection biases of existing ground-based surveillance systems and is not a neutral sample of the LEO population. Second, the LEO population is growing and evolving rapidly, and a design tied to the current catalog distribution would risk obsolescence. Third, equal-weight evaluation guarantees a robustness floor: all orbital types are equally covered, regardless of their current population density.

Table 5. Comparison of coverage predictions under uniform sampling in the two frameworks.

Framework	Predicted Coverage (%)	TLE Actual (%)	Error (pp)
Uniform in 3D space ($w \propto a^2 \lvert \cos i \rvert$ in orbital space)	7.03	0.86	+6.17
Uniform in 4D orbital space (equal weights)	5.47	0.86	**+4.61**

In summary, spherical-shell (3D spatial) and phase-space (4D orbital) are two distinct evaluation paradigms that yield different coverage predictions because they adopt different definitions of uniformity. The key difference is not that one is inherently "more accurate" than the other—both overestimate the coverage of a non-uniform real catalog, as expected—but that the phase-space framework provides orbit-type-resolved diagnostic capability. By evaluating coverage in the same (a, i, Ω, u) space where constellation design parameters (altitude, inclination, Walker configuration) reside, phase-space evaluation enables coverage results to directly inform design decisions with orbital-type granularity.

All constellation design and optimization in the following sections adopt the phase-space (4D orbital) framework with equal-weight evaluation as the baseline.

4.2. SSO Satellite Altitude Optimization

According to the optimization workflow of Section 3 (Figure 4, Stage 1), DE camera pointing optimization is first performed at each of 8 SSO altitudes (600–2500 km). The engineering baseline is set at $n_{cam} = 5$, a typical payload configuration for this class of optical surveillance satellite. The optimization computes the single-satellite equal-weight phase-volume coverage $P_{vol}(h)$, as reported in Table 6.

Table 6. Phase-volume coverage as a function of SSO satellite altitude.

SSO Altitude (km)	Inclination (°)	Phase-Volume Coverage (%)	DE Evaluations	DE Time (s)
600	97.8	19.74	600	44
800	98.6	18.22	450	31
1000	99.5	17.62	360	26
1200	100.4	19.09	240	17
1500	102.0	21.10	600	45
1700	103.1	23.72	450	33
2000	104.9	21.64	450	32
2500	108.3	16.17	330	28

Two trends emerge from the altitude sweep (see Figure 7):

1. The equal-weight phase-volume coverage peaks at 1700 km (23.72%). Coverage initially decreases from 19.74% at 600 km to 17.62% at 1000 km (FOV footprint limited at near-Earth altitudes), then rises to the optimum at 1700 km (increased altitude expands the FOV footprint on the target orbital shell), and declines beyond 2000 km (increased target range reduces the FOV angular coverage of a given target region), reaching 16.17% at 2500 km. (Note: All eight SSO altitudes underwent the same DE

pointing optimization procedure with identical population size, generation count, and grid resolution. The 23.72% coverage at 1700 km is the result of this procedure.) At the optimal altitude of 1700 km, a five-seed DE robustness test yields a run-to-run standard deviation of approximately 1.8 pp, confirming that the optimization is robust to random initialization.

2. The preferred altitude of 1700 km achieves the best balance between FOV footprint size and target range within the geometric visibility model used in this study. The current visibility model is purely geometric (Earth occultation, Earth shadow, solar angle, FOV, and angular rate constraints). Radiometric factors such as target magnitude, albedo, exposure time, and SNR are not modeled. For a comprehensive treatment of radiometric detectability modeling for space-based optical sensors, see, e.g., Campiti et al. [36]. Incorporating a radiometric detectability model would provide a more complete physical basis for the altitude optimum and is recommended as future work. This altitude serves as both the baseline orbital altitude for the subsequent constellation configuration sweep and is consistent with the operational altitude range of existing SSO surveillance satellites.

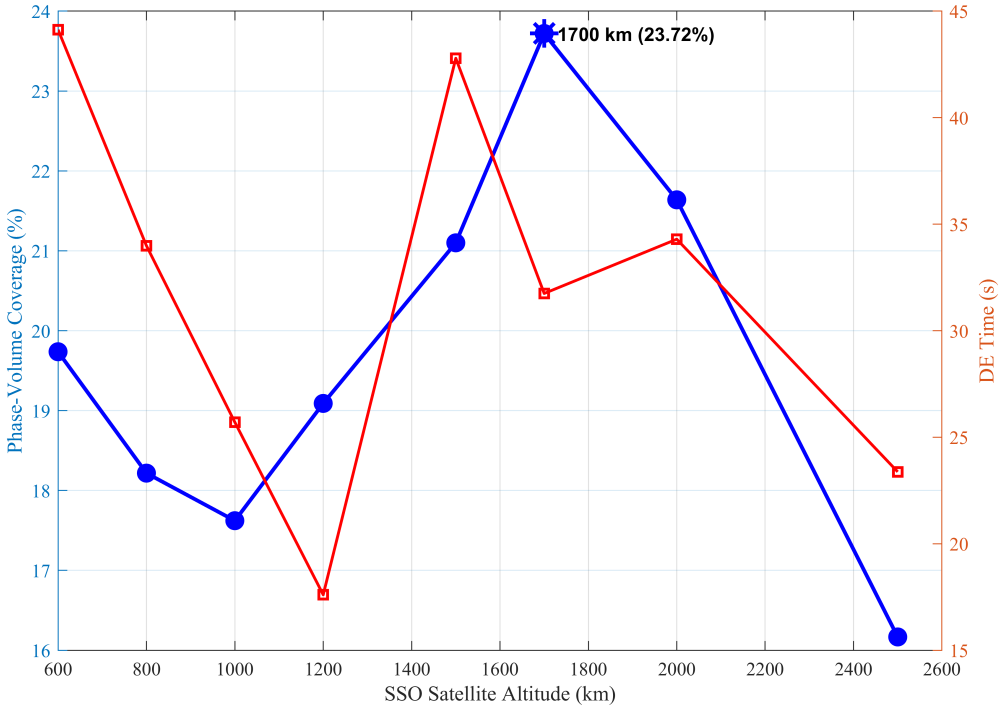


Figure 7. Influence of SSO satellite altitude on phase-volume coverage: coverage peaks at 1700 km, reflecting the geometric trade-off between FOV footprint size and target range.

The non-monotonic coverage–altitude relationship reflects a fundamental geometric trade-off. At lower altitudes, the FOV footprint on the target orbital shell is small, limiting the probability of intersecting a target. At higher altitudes, the increased slant range reduces the solid angle subtended by the FOV at the target distance, decreasing the effective coverage per camera pointing. The preferred altitude of 1700 km sits at the intersection of these two competing geometric effects, and is, therefore, adopted as the baseline for all subsequent optimization steps.

To verify that the altitude preference is not an artifact of the grid discretization, a sensitivity analysis was conducted at $h = 1700$ km with four (Ω, u) grid resolutions from 12×12 to 36×36 (Table 7). The phase-volume coverage varies by only 1.40 pp across this fourfold range, confirming that the altitude ranking is insensitive to the choice of grid resolution.

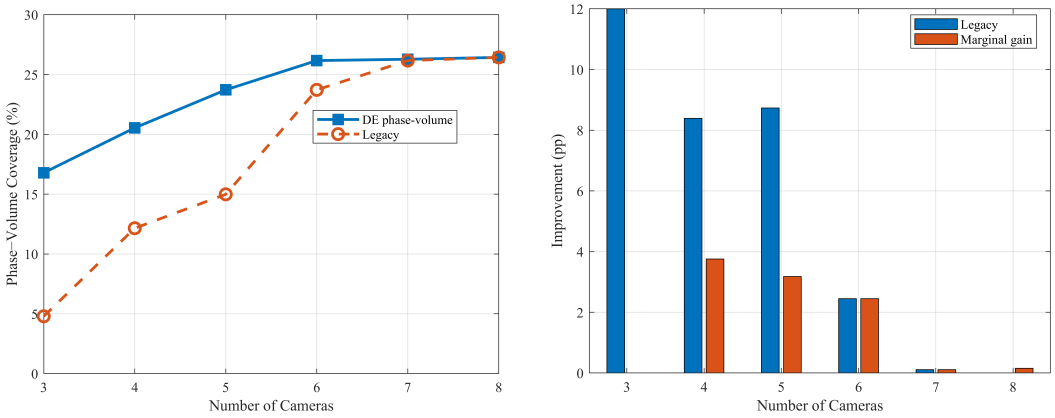
Table 7. Grid resolution sensitivity of phase-volume coverage at $h = 1700$ km.

Grid Size ($\Omega \times u$)	P_{vol} (%)
12×12	22.32
18×18	22.64
24×24	23.18
36×36	23.72
Range	1.40 pp

4.3. Camera Count and Pointing Optimization

After determining the optimal altitude $h^* = 1700$ km, DE pointing optimization is performed at this altitude for $n_{cam} \in \{3, 4, 5, 6, 7, 8\}$ (Figure 4, Stage 2) to validate the $n_{cam} = 5$ baseline. The optimization objective is maximization of equal-weight phase-volume coverage P_{vol}.

Figure 8 presents the camera count optimization results and Table 8 lists the numerical outcomes. Figure 9 shows the five-camera installation configuration: Figure 9a 3D perspective view, Figure 9b V-Nadir side view, and Figure 9c V-Cross top-down view. Each camera has a square FOV of $20° \times 20°$ (half-angle $10°$). Cameras C1–C4 cover the upper hemisphere and C5 covers the lower hemisphere.

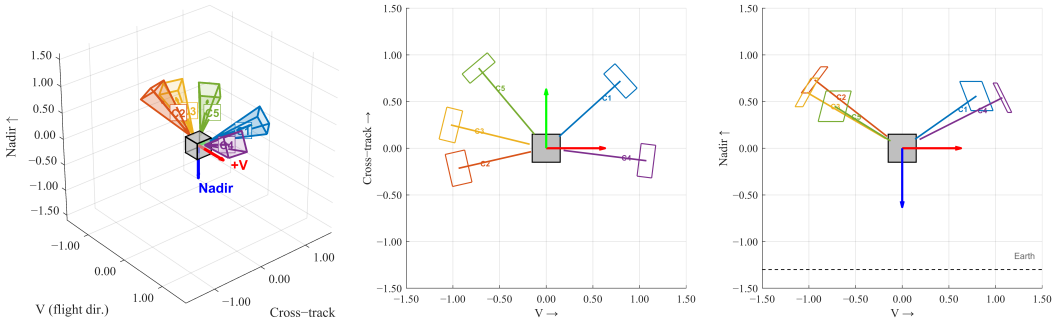


(**a**) (**b**)

Figure 8. Camera count optimization results. (**a**) Coverage vs. camera count. (**b**) Improvement vs. legacy and marginal gain.

Table 8. Camera count and pointing optimization results.

Camera Count	DE Phase-Volume Optimized (%)	Marginal Gain (pp)	DE Time (s)
3	16.79	—	31
4	20.54	+3.75	48
5	23.72	+3.18	68
6	26.17	+2.45	87
7	26.28	+0.11	56
8	26.43	+0.15	47



(**a**) (**b**) (**c**)

Figure 9. Five-camera installation schematic: cameras C1–C4 cover the upper hemisphere and C5 covers the lower hemisphere, providing near-complete spherical coverage with only five cameras. (**a**) 3D perspective view. (**b**) V-Nadir side view. (**c**) V-Cross top-down view.

The optimization exhibits a clear saturation behavior:

1. As the camera count increases from three to six, DE phase-volume coverage grows continuously and significantly (+9.38 pp). Beyond 6, marginal returns collapse: 6→7 adds only 0.11 pp, 7→8 adds only 0.15 pp. Six cameras represent the convergence point for pure coverage performance.
2. With DE optimizing phase-volume coverage, the five-camera configuration achieves 23.72% (baseline), and six cameras further improves to 26.17% (+2.45 pp, a 10.3% increase). Balancing coverage gain against engineering constraints (mass, power, data rate), five cameras is adopted as the practical configuration choice.
3. The optimal camera count from a pure coverage perspective is 8 (26.43%), but the marginal gain from six to eight cameras is only 0.26 pp. Adding two cameras yields almost no additional coverage benefit, indicating that the upper hemisphere is already adequately covered by six cameras.

The rapid saturation above six cameras confirms that the marginal benefit of additional cameras is dominated by the diminishing returns of overlapping FOVs. The five-camera configuration is selected for the subsequent analysis: it achieves 90% of the eight-camera optimum coverage with 38% fewer cameras, representing the best engineering compromise between coverage performance and payload complexity.

4.4. Influence of Constellation Configuration on Phase-Volume Coverage

With the altitude ($h^* = 1700$ km) and camera configuration (five cameras) determined, the next step is to sweep the Walker-Delta constellation parameters. This corresponds to Stage 3 of the optimization workflow (Figure 4). The design variables are the number of planes P, the number of satellites per plane S, and the phasing factor F. The total satellite count is $T = P \times S$. For each configuration, the equal-weight phase-volume coverage P_{vol} is computed under the same DE-optimized camera pointing.

The constellation parameter space is defined as $P \in \{1, 2, 3, 4, 6\}$ and $S \in \{1, 2, 3, 4, 6\}$, with $F \in [0, P-1]$. From the full combinatorial space of $5 \times 5 = 25$ (P, S) pairs, the only excluded combination is $P = 6$, $S = 6$ ($T = 36 > 30$). For each of the remaining 24 (P, S) pairs, all integer phasing factors $F = 0, 1, \ldots, P-1$ were evaluated, yielding 74 configurations in total.

The sweep covers a total satellite count range of $T = 8$–24, producing a coverage landscape over the (P, T, F) space. Figure 10 visualizes this landscape, and Table 9 lists the top nine configurations.

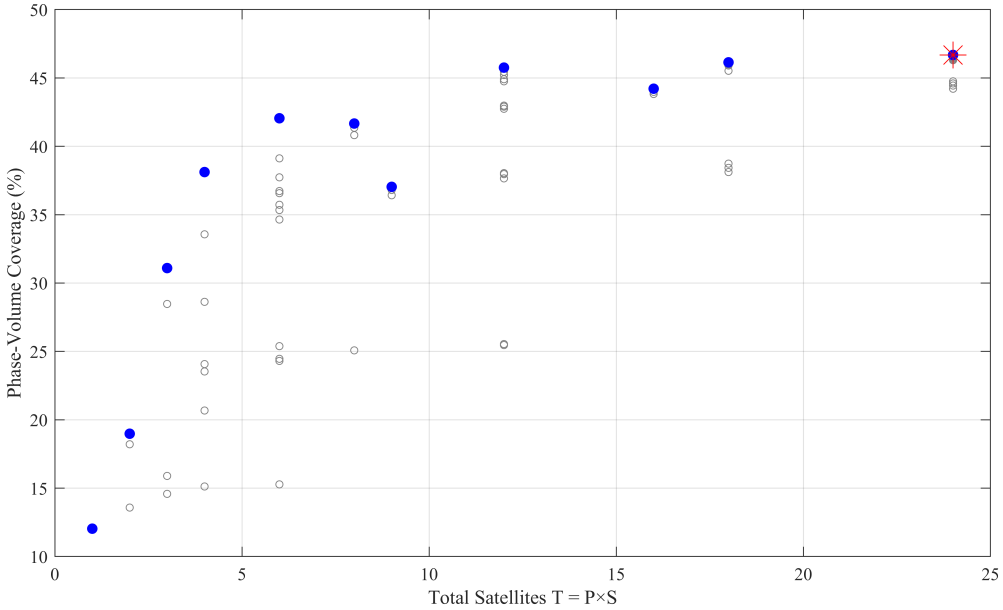


Figure 10. Constellation configuration sweep: $P = 6$-plane layouts consistently dominate, with coverage saturating at $T \geq 18$; beyond this point, adding satellites primarily improves observation geometry quality rather than coverage extent.

Table 9. Top nine constellation configurations from the sweep (sorted by phase-volume coverage).

Rank	*P*	*S*	*T*	*F*	Phase-Volume Coverage (%)
1	6	4	24	1	46.68
2	6	4	24	0	46.60
3	6	4	24	3	46.53
4	6	4	24	4	46.45
5	6	4	24	5	46.37
6	6	4	24	2	46.30
7	6	3	18	1	46.14
8	6	3	18	2	46.06
9	6	3	18	4	45.99

The sweep reveals a strong and consistent preference for six-plane layouts:

1. All top nine configurations have $P = 6$ planes, demonstrating that the six-plane layout significantly outperforms other plane counts.
2. For the same $T = 24$, the coverage difference between the best $F = 1$ and the worst $F = 2$ is 0.38 pp. Tuning the phasing factor F remains practically meaningful, though its influence is far smaller than that of the total satellite count T.
3. The coverage range of the top nine is only 0.69 pp (45.99–46.68%), and coverage saturates for $T \geq 18$ (coverage increases by only 0.54 pp from $T = 18$ to $T = 24$). This indicates that adding more satellites primarily improves OD quality metrics. At this point, the discriminative power of OGQI becomes more important.
4. Integrating coverage and OD quality, the $T = 24$ configuration ($P = 6, S = 4, F = 1$) is selected for subsequent TLE validation. It achieves 95.49% time-domain coverage on the real target population.

The consistent dominance of $P = 6$ configurations across all T and F values indicates that the six-plane layout is a robust structural optimum for SSO Walker-Delta constellations, independent of specific phasing or satellite count. As coverage saturates beyond $T = 18$, the design problem transitions from maximizing coverage to optimizing OD quality, a task for which OGQI provides the necessary discriminative power.

4.5. Observation Geometry Quality Index Analysis

The constellation sweep (Section 4.4) identified several configurations with near-identical phase-volume coverage. When coverage saturates, it can no longer discriminate among candidate designs. This motivates the use of OGQI (Equation (10)), which integrates phase-volume coverage P_{vol}, multi-coverage ratio R_{multi}, and mean covering satellite count $\bar{N}_{sat}$ into a single metric. OGQI captures not only whether a target is covered, but also the quality of that coverage for orbit determination. Table 10 presents the OGQI-based re-ranking of the top nine configurations from the sweep, alongside the raw coverage ranking for comparison.

The σ_{rel} values range from 0.4308 to 0.4314 across all configurations, indicating that the relative coverage non-uniformity across (a, i) bins is similar for all $P = 6$ layouts. This near-constant σ_{rel} is expected: all top-ranked configurations share six-plane $(P = 6)$ Walker geometries with similar satellite counts ($T = 18$ or $T = 24$). Since σ_{rel} measures the relative dispersion of coverage across (a, i) bins, configurations with the same number of orbital planes and similar total satellite counts produce comparable spatial coverage uniformity. Consequently, σ_{rel} carries limited discriminative weight in the OGQI ranking among the top configurations, where the ranking is driven primarily by R_{multi} and $\bar{N}_{sat}$. The OGQI-based ranking reorders the top configurations and exposes a coverage–precision trade-off:

1. The configuration with the highest coverage ($F = 1$, PV = 46.68%) is not the OGQI-optimal one. The OGQI optimum is $F = 0$ (OGQI=0.5165, $R_{multi} = 64.5\%$), due to its higher multi-coverage ratio (64.5% vs. 62.9%). Ranking by coverage alone would miss this distinction.
2. The OGQI of $T = 24$ configurations (0.5102–0.5165) is significantly higher than that of $T = 18$ (0.4989–0.5050), and the difference arises primarily from $\bar{N}_{sat}$ (3.0–3.2 vs. 2.3–2.4) rather than coverage.
3. The OGQI variation within the $P = 6$ group is only about 1.2% (0.5102–0.5165), indicating that the F factor has less influence on OD quality than the total satellite count T.
4. The coverage difference among $T = 24$ configurations with different F factors is only 0.38 pp (46.30%–46.68%), which is smaller than the grid resolution uncertainty of 1.40 pp (Table 7). Therefore, the ranking among individual F values should be interpreted with caution. The distinction between $T = 24$ and $T = 18$ groups (coverage difference $\sim$0.7 pp) is also within this uncertainty band, but the OGQI difference between these groups ($\sim$0.01, or $\sim$2%) is larger than the σ_{rel} variation and reflects a real improvement in observation geometry quality driven by the higher $\bar{N}_{sat}$.
5. The above results are based on the five-camera configuration. The camera count optimization demonstrates that five cameras achieve the optimal balance between coverage performance and engineering feasibility (Sections 4 and 4.3).

Table 10. Comparison of observation geometry quality metrics.

P	S	T	F	PV (%)	R_{multi} (%)	$\bar{N}_{sat}$	OGQI	σ_{rel}
6	4	24	0	46.60	64.5	3.16	0.5165	0.4308
6	4	24	3	46.53	64.1	3.15	0.5150	0.4308
6	4	24	1	46.68	62.9	2.99	0.5135	0.4311
6	4	24	4	46.45	63.8	3.16	0.5134	0.4310
6	4	24	5	46.37	63.3	3.08	0.5114	0.4308
6	4	24	2	46.30	63.1	3.11	0.5102	0.4309
6	3	18	1	46.14	61.1	2.43	0.5050	0.4314
6	3	18	2	46.06	58.4	2.34	0.4989	0.4313
6	3	18	4	45.99	60.4	2.38	0.5020	0.4313

To assess the robustness of the OGQI-based ranking to the choice of weighting coefficients, a sensitivity analysis was conducted by varying α and β by $\pm 30\%$ around their baseline values ($\alpha = 0.5$, $\beta = 0.3$). Across all nine combinations ($\alpha \in \{0.35, 0.50, 0.65\}$, $\beta \in \{0.21, 0.30, 0.39\}$), the configuration $F = 0$ ($P = 6, S = 4, T = 24$) consistently ranked first, demonstrating that the optimal configuration selection is insensitive to reasonable variations in the designer's trade-off preferences. This robustness conclusion applies to the tested $\pm 30\%$ range of (α, β) and should not be extrapolated to arbitrary weight variations outside this range without additional analysis.

Figure 11 further presents the coverage distribution and multi-coverage ratio heatmap in (a, i) space for the OGQI-optimal configuration ($F = 0$, OGQI = 0.5165). The coverage distribution exhibits pronounced spatial non-uniformity. SSO satellites achieve significantly higher coverage for high-inclination targets ($i > 70^\circ$) than for low-inclination targets. Note that this is a constellation-level result (24 satellites). In the single-satellite diagnostic of Section 4.1, the phase-volume coverage was found to be lowest near $i \approx 70^\circ$. The constellation design compensates for this single-satellite weakness: with multiple satellites in coordinated planes, the high-inclination region benefits from frequent orbital plane intersections with the SSO satellites, resulting in high cumulative coverage. The two findings are obtained at different scales (single satellite vs. 24-satellite constellation) and are not contradictory. Coverage also varies non-monotonically with target altitude, peaking near the satellite altitude (1500–2000 km) and declining for targets far below or above this altitude. Coverage ratios can differ by a factor of several across different (a, i) regions. This non-uniformity is precisely the spatial foundation for OGQI's continued discriminative power after top nine coverage saturates (Sections 4 and 4.4). The multi-coverage ratio R_{multi} essentially measures the degree of coverage overlap in (a, i) space.

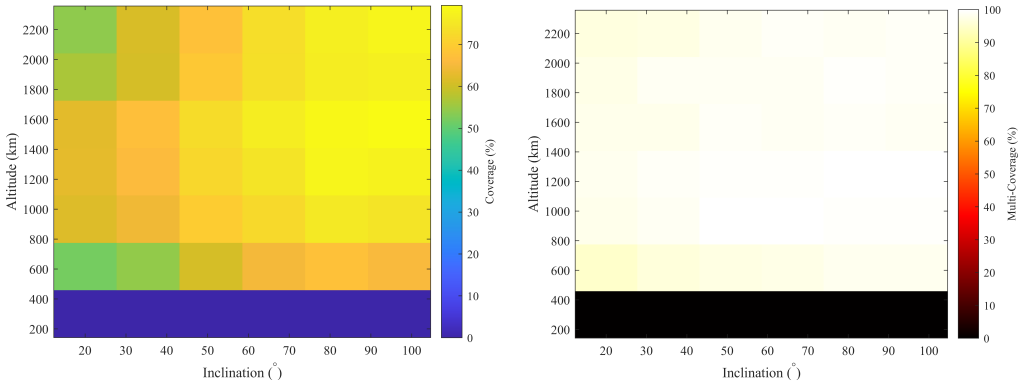


Figure 11. Coverage distribution and multi-coverage ratio heatmap in (a, i) space for the optimal configuration ($T = 24$, $P = 6$, $S = 4$, $F = 0$). (**a**) Phase-volume coverage ratio by orbital type. (**b**) Multi-coverage ratio R_{multi} by orbital type.

4.6. TLE Validation Against Real Target Population

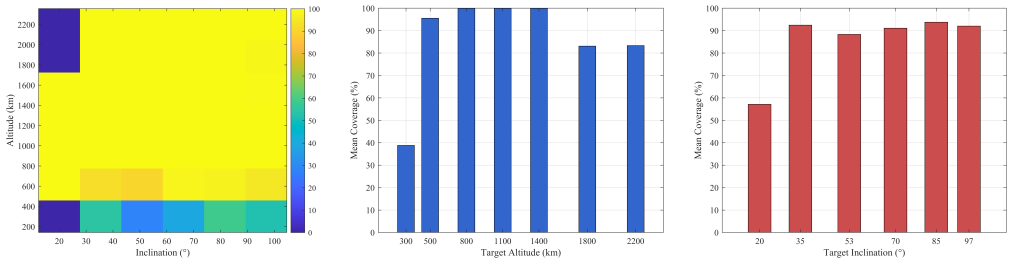
The preferred constellation configuration (Walker $P = 6$, $S = 4$, $T = 24$, $F = 1$, $h = 1700$ km SSO, 5 cameras with DE-optimized pointing) is validated in the time domain against all LEO targets in the public TLE catalog downloaded from the Space-Track website on 3 March 2026. (Note: $F = 1$ achieves the highest phase-volume coverage (46.68%), while $F = 0$ is OGQI-optimal (0.5165). Since the primary objective of TLE validation is coverage evaluation, $F = 1$ is selected.) Targets are propagated via the SGP4 propagator to a 1-h window following the reference epoch (time step $\Delta t = 10$ s, 361 steps total), using the same visibility model as the phase-volume framework (including all 8 constraints: Earth shadow, Earth occultation, 5° Earth albedo avoidance, FOV 20° × 20°, angular rate 3–120 pix/s,

etc.). A target is declared covered if it is continuously visible to at least one satellite in the constellation for at least 10 s (≥2 consecutive sample steps).

Table 11 summarizes the TLE validation metrics, and Figure 12 presents the coverage distributions for the real target population. Figure 12a shows the coverage ratio heatmap grouped by orbital type (a, i). Figure 12b,c show the marginal coverage distributions by altitude and inclination, respectively.

Table 11. TLE validation results for the real target population.

Metric	Value
Total TLE targets	22,471
Coverage ratio (≥1 satellite, ≥10 s)	95.49%
Multi-coverage ratio (≥2 satellites)	83.47%
Mean number of covering satellites	2.56
Maximum number of covering satellites	7
TLE Observation Geometry Quality Index (OGQI)	1.3060



(**a**) (**b**) (**c**)

Figure 12. TLE validation results for the real target population. (**a**) Coverage ratio heatmap by orbital type (a, i). (**b**) Marginal coverage distribution by altitude. (**c**) Marginal coverage distribution by inclination.

It is important to clarify the relationship between the two evaluations. The phase-volume coverage P_{vol} is a static, instantaneous, equal-weight metric computed over the entire (a, i, Ω, u) target space. The TLE validation is a dynamic, 1-h cumulative metric evaluated against the actual catalog, which has a highly non-uniform orbital distribution. A direct numerical comparison between the two is, therefore, not meaningful: the phase-volume result (∼46%) reflects equal weighting across all orbital types, while the TLE result (95.49%) reflects both the 1-h time accumulation and the concentration of real targets in well-covered orbital regions. The two evaluations serve complementary roles. Phase-volume evaluation ensures design robustness: no orbital type is overlooked, and coverage shortfalls in specific (a, i) regions are directly diagnosable. TLE validation confirms that the designed constellation achieves effective real-world coverage against the current target population. Together they provide a more complete assessment than either alone. It should also be noted that the TLE validation assesses 1-h cumulative visibility, which is a coverage metric. It does not constitute orbit determination (OD) performance verification. Observing a target once does not establish orbit convergence or sustained custody. Full OD performance validation through multi-epoch angles-only Monte Carlo simulation is deferred to future work.

Additionally, to assess the temporal stability of the coverage result, validation was repeated using a second TLE catalog snapshot from 15 July 2026 (23,171 LEO objects). The coverage from the two snapshots is consistent: 95.49% (3 March) vs. 94.47% (15 July), a difference of 1.02 pp. The multi-coverage ratio shows a larger change (83.47% vs. 77.10%), reflecting the varying composition of the TLE catalog between the two epochs.

The TLE validation confirms the design's effectiveness against the real target population:

1. The constellation achieves 95.49% coverage of the 22,471 real LEO targets within the phase-volume domain, with 83.47% of covered targets observable by $\geq$2 satellites simultaneously (multi-coverage), providing favorable triangulation conditions. This result validates the effectiveness of the phase-volume optimization conclusions on the real target population.
2. The coverage shortfall primarily occurs in the $h = 300$ km low-altitude region (some target groups have coverage $< 60\%$), because low-altitude targets have higher orbital angular rates and shorter visibility windows, making them more sensitive to the dwell time constraint. Target groups at $h \geq 500$ km achieve near-100% coverage.
3. The constellation achieves significantly higher coverage for targets with $i > 70^\circ$ than for low-to-mid-inclination targets, consistent with the static coverage map in Section 4.5. This reflects two effects: (a) SSO satellites at $i_G \approx 97^\circ$–100° have natural geometric favorability for high-inclination targets, and (b) the 1-h time window provides more cumulative observation opportunities for high-inclination targets whose orbital planes intersect the satellite's coverage zone more frequently.
4. The TLE target OGQI of 1.3060 is significantly higher than the OGQI of the top phase-volume configurations (0.5165). Real targets are heavily concentrated in the $h = 500$–800 km region (71.8% of the catalog), which is precisely the altitude band where the constellation's coverage is optimal. The optimized constellation's coverage advantage region coincides with the target density peak.
5. The TLE coverage (95.49%) is far higher than the phase-volume constellation coverage ($\sim$46%). This discrepancy is expected, arising from two fundamental differences between the evaluation paradigms:
   - Evaluation domains. Phase-volume uniformly samples the entire (a, i, Ω, u) space, including extreme orbits where the constellation's coverage is inherently weak (e.g., $h = 300$ km, $i \approx 20^\circ$ low-inclination near-Earth targets with extremely short visibility windows). The TLE catalog is heavily concentrated in the $h = 500$–800 km, mid-to-high-inclination region, which is precisely the SSO constellation's coverage advantage zone.
   - Time dimensions. Phase-volume is a single-epoch snapshot: each (Ω, u) point is evaluated at only one instant. TLE validation uses a 1-h time window (361 sample steps). The time window allows targets to traverse a large fraction of their orbit, passing through multiple satellite coverage zones and substantially increasing the probability of being covered.

   The two are complementary: phase-volume ensures design robustness (no orbital type is overlooked), while TLE validation provides real-world effectiveness (performance against the actual target population).

Taken together, the TLE validation demonstrates that the phase-volume-optimized constellation design generalizes effectively to the real LEO target population. The design transfers from the uniform (a, i, Ω, u) evaluation space to a non-uniformly distributed catalog without performance loss. The 95.49% time-domain coverage was achieved without any catalog-specific tuning. This confirms that the design methodology yields a constellation that is both theoretically rigorous and practically effective. The methodology consists of three steps: altitude selection via phase-volume sweep, camera optimization via DE, and configuration selection via OGQI.

5. Conclusions

This paper has presented a systematic constellation optimization methodology based on phase-volume coverage and observation geometry quality. Building on the Ω-u phase-plane method of Wu et al. [30], the phase-volume framework extends the evaluation domain from two to four orbital elements (a, i, Ω, u), enabling unified coverage assessment over the LEO target space. The main findings are as follows.

Spherical-shell 3D spatial sampling and phase-space 4D orbital sampling are two distinct evaluation paradigms connected by the Jacobian factor $\propto a^2|\cos i|$. They adopt different definitions of uniformity—spatial isotropy versus orbital-type equal weighting—and, therefore, yield different coverage predictions. The defining advantage of the phase-space framework is its orbit-type-based diagnostic capability: coverage shortfalls can be directly mapped to specific (a, i) regions and addressed through targeted constellation design, a capability unavailable in spatial methods.

The SSO altitude sweep shows that, with $n_{cam} = 5$ as the engineering baseline, equal-weight phase-volume coverage peaks at 1700 km (23.72%). Camera count validation at this altitude confirms that five cameras achieve the optimal balance between coverage gain (3→5: +6.93 pp) and marginal returns (5→6: +2.45 pp, with <0.3 pp beyond 6), validating the engineering baseline selection. The constellation configuration sweep demonstrates that $P = 6$-plane layouts significantly outperform other configurations, with all top nine candidates belonging to $P = 6$. Coverage saturates for $T \geq 18$, beyond which adding satellites primarily improves observation geometry quality rather than coverage extent.

The observation geometry quality metrics (R_{multi}, $\bar{N}_{sat}$, OGQI) complement single-metric coverage evaluation by incorporating multi-satellite observation geometry into the design criterion. Fisher information matrix theory provides a qualitative motivation for each OGQI component: R_{multi} reflects the fraction of targets with triangulation-capable multi-satellite geometry, and $\bar{N}_{sat}$ represents observation redundancy. However, the relationship between OGQI and actual OD accuracy should be understood as a positive correlation rather than a strict mathematical equivalence. The Fisher analysis offers physical insight into why multi-coverage and observation redundancy matter. Among the top nine configurations, the highest-coverage configuration ($F = 1$, 46.68%) is not OGQI-optimal; $F = 0$ achieves the highest OGQI (0.5165) through a higher multi-coverage ratio. A sensitivity analysis confirms that the OGQI ranking is robust to ±30% variations in the weighting coefficients. TLE validation against the Space-Track public catalog (22,471 LEO objects) with the final optimized constellation achieves 95.49% coverage and 83.47% multi-coverage within a 1-h window, with a second TLE snapshot (15 July 2026) confirming temporal stability (coverage 95.49% vs. 94.47%, difference 1.02 pp). This validation assesses 1-h cumulative visibility (coverage) and does not constitute OD performance verification, which requires multi-epoch OD simulation.

Several directions merit further investigation. First, empirical weighting of the phase-space using the actual TLE target distribution can bring phase-volume predictions closer to catalog-based coverage, pending the development of methods to avoid embedding existing catalog selection biases into the design. Second, multi-epoch angles-only OD Monte Carlo simulation with realistic measurement noise models is needed to validate the correlation between OGQI rankings and actual OD accuracy established theoretically in Section 2. Third, the current sequential optimization of camera pointing and constellation configuration may be replaced by joint co-optimization of (P, S, F) and per-satellite camera pointing driven by a compound objective function. Fourth, cooperative networking of SSO and inclined-orbit constellations can be explored to evaluate the complementary effect of multi-plane combinations on full-LEO-space coverage.

Author Contributions: Conceptualization, X.W.; methodology, X.W. and P.C.; software, X.W.; validation, X.W. and P.C.; formal analysis, X.W.; data curation, X.W.; writing—original draft preparation, X.W.; writing—review and editing, P.C. All authors have read and agreed to the published version of the manuscript.

Funding: This research was supported by the Fundamental Research Funds for the Central Universities of China under Grant 501XSKC2025115001.

Institutional Review Board Statement: Not applicable.

Informed Consent Statement: Not applicable.

Data Availability Statement: The TLE data used in this study are publicly available from the Space-Track website (https://www.space-track.org, accessed on 15 July 2026). The simulation code can be made available upon reasonable request to the corresponding author.

Acknowledgments: The authors gratefully acknowledge Space-Track for providing the TLE data used in the validation.

Conflicts of Interest: The authors declare no conflicts of interest.

Abbreviations

The following abbreviations are used in this manuscript:

LEO	Low Earth Orbit
SSO	Sun-Synchronous Orbit
OD	Orbit Determination
OGQI	Observation Geometry Quality Index
DE	Differential Evolution
TLE	Two-Line Element
VVLH	Vehicle Velocity Local Horizontal
FOV	Field of View
SSA	Space Situational Awareness
ATH	Above the Horizon

Appendix A. Derivation of the Jacobian for the $(a, i, \Omega) \mapsto (x, y, z)$ Mapping at Fixed u

This appendix provides the step-by-step derivation of the Jacobian determinant $\mathcal{J} = |\partial(x, y, z)/\partial(a, i, \Omega)|_{u\,\text{fixed}}$ referenced in Section 2.

From Equation (4), the position vector at fixed u for a circular orbit is $\mathbf{r} = a \cdot R_z(\Omega)R_x(i)[\cos u,\ \sin u,\ 0]^\top$, where

$$R_z(\Omega) = \begin{bmatrix} \cos\Omega & -\sin\Omega & 0 \\ \sin\Omega & \cos\Omega & 0 \\ 0 & 0 & 1 \end{bmatrix}, \qquad R_x(i) = \begin{bmatrix} 1 & 0 & 0 \\ 0 & \cos i & -\sin i \\ 0 & \sin i & \cos i \end{bmatrix}.$$

The 3×3 Jacobian $\mathbf{J} = [\mathbf{j}_1, \mathbf{j}_2, \mathbf{j}_3]$ has columns $\mathbf{j}_1 = \partial\mathbf{r}/\partial a$, $\mathbf{j}_2 = \partial\mathbf{r}/\partial i$, $\mathbf{j}_3 = \partial\mathbf{r}/\partial\Omega$.

Column 1. $\mathbf{j}_1 = \partial\mathbf{r}/\partial a = R_z R_x[\cos u, \sin u, 0]^\top = \mathbf{r}/a$.

Column 2. $\mathbf{j}_2 = \partial\mathbf{r}/\partial i = aR_z\,(dR_x/di)\,[\cos u, \sin u, 0]^\top$. The derivative of $R_x(i)$ is $\frac{dR_x}{di} = \begin{bmatrix} 0 & 0 & 0 \\ 0 & -\sin i & -\cos i \\ 0 & \cos i & -\sin i \end{bmatrix}$, yielding $[0, -\sin i \sin u, \cos i \sin u]^\top$ after application to the vector.

Column 3. $\mathbf{j}_3 = \partial\mathbf{r}/\partial\Omega = a\,(dR_z/d\Omega)\,R_x[\cos u, \sin u, 0]^\top$. The derivative of $R_z(\Omega)$ is $\frac{dR_z}{d\Omega} = \begin{bmatrix} -\sin\Omega & -\cos\Omega & 0 \\ \cos\Omega & -\sin\Omega & 0 \\ 0 & 0 & 0 \end{bmatrix}$. Observe that this is the cross-product matrix: $\mathbf{j}_3 = \mathbf{k} \times \mathbf{r}$ with $\mathbf{k} = [0, 0, 1]^\top$.

Evaluating the determinant. For a 3×3 matrix, $\det \mathbf{J} = \mathbf{j}_1 \cdot (\mathbf{j}_2 \times \mathbf{j}_3)$ (scalar triple product). Substituting the column expressions and using $\mathbf{j}_3 = \mathbf{k} \times \mathbf{r}$:

$$\det \mathbf{J} = \frac{\mathbf{r}}{a} \cdot \big(\mathbf{j}_2 \times (\mathbf{k} \times \mathbf{r})\big).$$

Apply the vector identity $\mathbf{a} \times (\mathbf{b} \times \mathbf{c}) = (\mathbf{a} \cdot \mathbf{c})\mathbf{b} - (\mathbf{a} \cdot \mathbf{b})\mathbf{c}$:

$$\mathbf{j}_2 \times (\mathbf{k} \times \mathbf{r}) = (\mathbf{j}_2 \cdot \mathbf{r})\mathbf{k} - (\mathbf{j}_2 \cdot \mathbf{k})\mathbf{r}.$$

Compute the two dot products:

- $\mathbf{j}_2 \cdot \mathbf{r} = 0$, because for a circular orbit $|\mathbf{r}| = a$ is constant with respect to i: differentiating $|\mathbf{r}|^2 = a^2$ gives $2\mathbf{r} \cdot (\partial \mathbf{r}/\partial i) = 0$.
- $\mathbf{j}_2 \cdot \mathbf{k} = a \cos i \sin u$, since R_z preserves the z-component and $(dR_x/di)[\cos u, \sin u, 0]^\top$ has z-component $\cos i \sin u$.

Thus $\mathbf{j}_2 \times (\mathbf{k} \times \mathbf{r}) = -(a \cos i \sin u)\,\mathbf{r}$. Finally:

$$\det \mathbf{J} = \frac{\mathbf{r}}{a} \cdot \big(-a \cos i \sin u\, \mathbf{r}\big) = -a^2 \cos i \sin u.$$

Taking the absolute value: $|\det \mathbf{J}| = a^2 |\cos i| \cdot |\sin u|$.

Interpretation. The Jacobian decomposes as $|\det \mathbf{J}| = a^2 |\cos i| \cdot |\sin u|$. This is a conditional result for fixed u and circular orbits. The $|\sin u|$ factor is u-periodic. Under the assumption that u is uniformly distributed over $[0, 2\pi)$, the mean value is $\mathbb{E}_u[|\sin u|] = \frac{1}{2\pi} \int_0^{2\pi} |\sin u|\, du = 2/\pi$, giving the averaged weighting factor $\bar{\mathcal{J}} \propto a^2 |\cos i|$ used in the phase-volume formulation (Section 2). This normalization assumes uniform sampling in u, which is consistent with the uniform gridding of the phase-volume. Different distributions of u would yield different averaging factors, but the qualitative dependence on $|\cos i|$ remains. The $|\cos i|$ factor shows that spatially uniform sampling over-samples equatorial orbits ($i \to 0^\circ$, $\cos i \to 1$) and under-samples polar orbits ($i \to 90^\circ$, $\cos i \to 0$), confirming that spatial uniformity is non-uniform in orbital element space.

References

1. Polli, E.M.; Gonzalo, J.L.; Colombo, C. Analytical model for collision probability assessments with large satellite constellations. *Adv. Space Res.* **2023**, *72*, 2515–2534. [CrossRef]
2. Mignocchi, A.; Rizzuto, S.S.; De Riz, A.; Montaruli, M.F. Advanced sensor tasking strategies for space object cataloging. *Aerospace* **2026**, *13*, 81. [CrossRef]
3. Jia, Q.; Xiao, J.; Bai, L.; Zhang, Y.; Zhang, R.; Feroskhan, M. Space situational awareness systems: Bridging traditional methods and artificial intelligence. *Acta Astronaut.* **2025**, *228*, 321–330. [CrossRef]
4. Hussain, K.F.; El-Din Safwat, N.; Thangavel, K.; Sabatini, R. Space-based debris trajectory estimation using vision sensors and track-based data fusion techniques. *Acta Astronaut.* **2025**, *229*, 814–830. [CrossRef]
5. Walker, J.G. Satellite constellations. *J. Br. Interplanet. Soc.* **1984**, *37*, 559–571.
6. Ballard, A.H. Rosette constellations of earth satellites. *IEEE Trans. Aerosp. Electron. Syst.* **1980**, *AES-16*, 656–673. [CrossRef]
7. Rider, L. Optimal orbital constellations for global viewing of targets against a space background. *Opt. Eng.* **1980**, *19*, 219–223. [CrossRef]
8. Hanson, J.M.; Linden, A.N. Improved low-altitude constellation design methods. *J. Guid. Control Dyn.* **1989**, *12*, 228–236. [CrossRef] [PubMed]
9. Dai, G.; Chen, X.; Wang, M.; Fernández, E.; Nguyen, T.N.; Reinelt, G. Analysis of satellite constellations for the continuous coverage of ground regions. *J. Spacecr. Rockets* **2017**, *54*, 1294–1303. [CrossRef]
10. Han, C.; Bai, S.; Zhang, S.; Wang, X.; Wang, X. Visibility optimization of satellite constellations using a hybrid method. *Acta Astronaut.* **2019**, *163*, 250–263. [CrossRef]
11. Zong, P.; Kohani, S. Optimal satellite LEO constellation design based on global coverage in one revisit time. *Int. J. Aerosp. Eng.* **2019**, *2019*, 1–12. [CrossRef]

12. He, X.; Li, H.; Yang, L.; Zhao, J. Reconfigurable satellite constellation design for disaster monitoring using physical programming. *Int. J. Aerosp. Eng.* **2020**, *2020*, 8813685. [CrossRef]
13. Yang, Y.; Wu, X.; Li, J.; Zgeib, R. Configuration design method of mega constellation for low earth orbit observation. *Space Sci. Technol.* **2024**, *4*, 0175. [CrossRef]
14. Wang, Z. On-Orbit Space AI Federated, Multi-Agent, and Collaborative Algorithms for Satellite Constellations. *Algorithms* **2026**, *19*, 318. [CrossRef]
15. Ali, I.; Al-Dhahir, N.; Hershey, J.E. Predicting the visibility of LEO satellites. *IEEE Trans. Aerosp. Electron. Syst.* **1999**, *35*, 1183–1190. [CrossRef]
16. Ji, H.; Zeng, G. A method for spatial effective coverage analysis in space-based optical observation. *Optik* **2018**, *166*, 116–126. [CrossRef]
17. Han, C.; Zhang, Y.; Bai, S.; Sun, X.; Wang, X. Novel method to calculate satellite visibility for an arbitrary sensor field. *Aerosp. Sci. Technol.* **2021**, *112*, 106668. [CrossRef]
18. Shakun, L.; Koshkin, N.; Korobeynikova, E.; Kozhukhov, D.; Kozhukhov, O.; Strakhova, S. Comparative analysis of global optical observability of satellites in LEO. *Adv. Space Res.* **2021**, *67*, 1743–1760. [CrossRef]
19. Roh, H.; De Weck, O.L. Global visibility assessment method of in-situ optics constellation for uncatalogued resident space objects. In Proceedings of the AIAA SCITECH 2025 Forum, Orlando, FL, USA, 6–10 January 2025.
20. Hu, Y.; Huang, J.; Chen, L. Space-based visible observation strategy for beyond-LEO objects based on an equatorial LEO satellite with multi-sensors. *Adv. Space Res.* **2017**, *59*, 1751–1762. [CrossRef]
21. Flohrer, T.; Krag, H.; Klinkrad, H.; Schildknecht, T. Feasibility of performing space surveillance tasks with a proposed space-based optical architecture. *Adv. Space Res.* **2011**, *47*, 1029–1042. [CrossRef]
22. Du, J.; Chen, J.; Li, B.; Sang, J. Tentative design of SBSS constellations for LEO debris catalog maintenance. *Acta Astronaut.* **2019**, *155*, 379–388. [CrossRef]
23. Du, J.; Lei, X.; Sang, J. A space surveillance satellite for cataloging high-altitude small debris. *Acta Astronaut.* **2019**, *157*, 268–275. [CrossRef]
24. Hu, Y.; Chen, L.; Huang, J. Space-based pseudo-fixed latitude observation mode based on the characteristics of geosynchronous orbit belt. *Acta Astronaut.* **2017**, *137*, 31–37. [CrossRef]
25. Biria, A.D.; Marchand, B.G. Constellation design for space-based space situational awareness applications: An analytical approach. *J. Spacecr. Rockets* **2014**, *51*, 545–562. [CrossRef]
26. Sun, Y.; Wen, C.; Zhang, C.; Zhu, Z.; Ye, Z. Above-the-horizon coverage for satellite constellations with dual-altitude band constraints using ring-based discretization. *J. Spacecr. Rockets* **2023**, *60*, 132–145. [CrossRef]
27. D'Anniballe, A.; Felicetti, L.; Hobbs, S. Preliminary analysis and design of an optical space surveillance and tracking constellation for LEO coverage. *Acta Astronaut.* **2025**, *231*, 47–63. [CrossRef]
28. Fu, Y.; Xu, Z.; Fan, Y.; Yi, L.; Ma, Z.; Li, Y.; Fang, S. Optimization of a Walker constellation using an RBF surrogate model for space target awareness. *Aerospace* **2025**, *12*, 933. [CrossRef]
29. Li, T.; Xiang, J.; Wang, Z.; Zhang, Y. Circular revisit orbits design for responsive mission over a single target. *Acta Astronaut.* **2016**, *127*, 219–225. [CrossRef]
30. Wu, X.; Mao, X.; Gong, Z.; Chen, P. Equal-probability group visibility criteria for orbit design of surveillance satellite. *Acta Astronaut.* **2026**, *239*, 113–127. [CrossRef]
31. Vallado, D.A. *Fundamentals of Astrodynamics and Applications*, 4th ed.; Microcosm Press: Hawthorne, CA, USA, 2013.
32. Gong, B.; Jiang, L.; Ning, X.; Li, S. Study on mission planning algorithm for multi-target passive tracking based on satellite formation. *Aerosp. Sci. Technol.* **2023**, *142*, 108660. [CrossRef]
33. Marchand, B.G.; Kobel, C.J. Above the horizon satellite coverage with dual-altitude band constraints. *J. Spacecr. Rockets* **2009**, *46*, 845–857. [CrossRef]
34. Luo, D.; Tao, X.; Zhang, Y. Optimal cislunar optical observation constellations design using orbit determination accuracy estimate. *Adv. Space Res.* **2026**, *77*, 10743–10776. [CrossRef]
35. Storn, R.; Price, K. Differential Evolution—A simple and efficient heuristic for global optimization over continuous spaces. *J. Glob. Optim.* **1997**, *11*, 341–359. [CrossRef]
36. Campiti, G.; Brunetti, G.; Ciminelli, C. Detectability of Potentially Colliding Space Objects via Star Trackers on at-Risk Satellites. *IEEE Trans. Aerosp. Electron. Syst.* **2025**, *61*, 11489–11511. [CrossRef]

Disclaimer/Publisher's Note: The statements, opinions and data contained in all publications are solely those of the individual author(s) and contributor(s) and not of MDPI and/or the editor(s). MDPI and/or the editor(s) disclaim responsibility for any injury to people or property resulting from any ideas, methods, instructions or products referred to in the content.